Uncertainties in Radiometer Intercalibration associated with Variability in Geophysical Parameters

John Xun Yang[1*], Darren S. McKague[1], and Christopher S. Ruf[1]

[1] Department of Climate and Space Sciences and Engineering, University of Michigan, Ann Arbor, MI

Corresponding author: John Xun Yang (johnxun@umich.edu)

Key Points:

- A ubiquitous periodic variation in radiometer intercalibration accuracy is detected and characterized
- The root cause of the variability is explained with an orbit model and a solution is proposed
- Intercalibration uncertainties are nonlinear, are not monotonic and are dependent on geophysical parameters

This is the author manuscript accepted for publication and has undergone full peer review but has not been through the copyediting, typesetting, pagination and proofreading process, which may lead to differences between this version and the Version of Record. Please cite this article as doi: 10.1002/2016JD024937

Abstract

Spaceborne radiometry plays a major role in weather and climate science and applications. Intercalibrating different radiometers has become an indispensable task for diagnosing instrument performance and integrating constellation data to extend the observational record. Because intercalibration affects both base radiance data and downstream science products, it is critical to examine intercalibration performance. In this study, we use constellation radiometer data from the Global Precipitation Measurement (GPM) mission to detect and characterize a pronounced variability in intercalibration stability with a ~40 day periodicity. A regional dependence of the calibration is also found. The variability is related to geophysical parameters including water vapor, surface wind speed, and sea surface temperature. It is found that the variability is caused by periodic variations in the local times and locations of the overlap regions between spacecraft. An analytical orbit model is developed for calculating the period of oscillation and agrees well with observation. Calibration errors show nonlinear and non-monotonic dependence on geophysical parameters and brightness temperature (TB), which cannot be removed by simple linear regression. The variability affects both base radiance calibration accuracy and retrieved science data products.

1. Introduction

Spaceborne microwave radiometers are a dominant instrument in weather and climate observations [*Joo et al.*, 2013; *Lorenc and Marriott*, 2014; *Ulaby and Long*, 2014]. They can measure important meteorological parameters such as precipitation, oceanic wind speed, atmospheric temperature and humidity and account for the dominant error reduction (~43%) in weather forecast from data assimilation among different spacecraft platforms [*Joo et al.*, 2013]. They not only perform measurements under clear-sky weather conditions, but also can see through clouds and precipitation with a near all-weather capability. Since an individual radiometer has limited temporal and spatial coverage, data are routinely combined from many radiometers. To do so, intercalibration is critical as it reconciles instrument differences at the base level of measured radiances and affects downstream science data products. Specifically, intercalibration can diagnose instrument performance issues [*Wentz et al.*, 2001; *Mo*, 2010; *McKague et al.*, 2011; *Qin et al.*, 2013; *Weng et al.*, 2013b], identify and correct scan dependent and scene brightness temperature dependent calibration errors as well as issues with the antenna pattern correction (APC) algorithm [*Yang et al.*, 2015], remove bias between different spacecrafts [*Yan and Weng*, 2008; *Berg et al.*, 2012; *Wilheit*, 2013; *Mo*, 2014], assist in developing next-generation instruments [*Wentz et al.*, 2001; *Draper et al.*, 2015a], and provide climate quality data [*Sapiano et al.*, 2013]. In this context, intercalibration is a subset of calibration and calibrates one target radiometer relative to another reference radiometer.

The intercalibrated radiances should ideally be error free. In reality, however, calibration is affected by a number of factors and residual errors are present despite calibration and intercalibration. Some errors are hardware related such as radiometer nonlinearity [*Weng et al.*, 2013b], main reflector emission [*Wentz et al.*, 2001; *Biswas et al.*, 2010; *Geer et al.*, 2010; *Yang et al.*, 2016a], and field of view (FOV) blockage

[*McKague et al.*, 2011; *Yang et al.*, 2016b]. Main reflector emission, for example, shows an orbit-dependent variability because the temperature of reflector is affected by solar illumination, which is dependent on the spacecraft orbital position [*Biswas et al*., 2010]. Some errors are due to modeling. In intercalibration, a radiative transfer model (RTM) and ancillary data representing geophysical fields are commonly used to estimate instrument performance [*Yan and Weng*, 2008; *McKague et al.*, 2011; *Sapiano et al.*, 2013; *Wilheit*, 2013; *Yang et al.*, 2014; *Yang and McKague*, 2016; *Yang et al.*, 2016b]. Simulation errors can be produced because of inaccurate empirical parameterization within the RTM [*Payne et al*., 2011; *Meissner and Wentz*, 2012] and biases in ancillary data [*Bengtsson et al*., 2007; *Kleist et al*., 2009]. The two different errors can be distinguished from each other as they exhibit different variability and dependence. For example, an emissive reflector exhibits temporal variability with a unique periodicity different from that of simulation errors because the variability of reflector temperature is dependent on spacecraft orbit and attitude [*Biswas et al*., 2010], while simulation errors often show regional dependence due to biases in reanalysis data that have regional difference. It is important to assess the uncertainties of intercalibration and differentiate error sources by examining the variability and dependence.

The NASA/JAXA Global Precipitation Measurement (GPM) mission uses a constellation of 15 spacecrafts for measuring global precipitation [*Hou et al.*, 2014]. The GPM core observatory carries on microwave imager (GMI), which is the transfer standard of all GPM radiometers. The GPM radiometers have different instrument design specifications such as frequency and EIA. Proper intercalibration should account for these differences as well as correct for known instrument errors (e.g., edge of scan obstructions, emissive reflector, solar intrusion on the warm load [*Wentz et al.*, 2001; *Ruf et al.*, 2006; *McKague et al.*, 2011; *Yang et al.*, 2015; *Yang et al.*, 2016b]. GPM provides a unique opportunity to investigate possible

intercalibration variability and dependence. The Interspacecraft Radiometer Calibration Working Group (XCAL) has been conducting extensive calibration work for GPM [*Wilheit*, 2013; *Wilheit et al.*, 2015; *Yang et al.*, 2015]. As a member of XCAL team, the group at University of Michigan has performed independent calibration studies and resolved a number of calibration issues [*Yang et al.*, 2015; *Yang and McKague*, 2016; *Yang et al.*, 2016b].

In this study, we investigate the variability of intercalibration accuracy and its dependence on geophysical parameters. The objective is to characterize any possible temporal or spatial variability, identify the underlying dependencies that affect radiometer data, differentiate simulation and instrument errors, and reduce intercalibration biases. We develop diagnostic methods that allow for a comprehensive characterization of calibration status. We present results for GMI and WindSat since the two radiometers have been well calibrated and show stable performance. Other five radiometers of GPM constellation have also been studied to verify the results. The findings apply in general for radiometer intercalibration as we verified with other constellation radiometers.

2. Data and Method

A brief summary of the intercalibration methodology is described here. More details can be found in companion work [*Yang et al.*, 2015; *Yang and McKague*, 2016; *Yang et al.*, 2016b] and in the appendix. In this study, intercalibration is based on collocating the field of view (FOV) from different radiometers. A RTM is used with ancillary reanalysis data to account for instrument differences in frequency, EIA, and bandwidth. The collocation requires the FOVs of two radiometers, the reference and target radiometer, to fall into a 0.1°×0.1° box within one hour. These collocation criteria have been compared to those of

previous studies and found to effectively minimize the impact of scene heterogeneity on intercalibration [*Yang and McKague*, 2016]. Clouds and precipitation are screened out with filters given in the appendix. Then, an RTM simulation is performed to simulate TBs corresponding to observations. As shown in the appendix, the single difference (SD) is defined as the difference of observed minus simulated TB for an individual radiometer. The double differenc**e** (DD) is the SD of the target radiometer minus that of the reference radiometer. Single differences are more sensitive to simulation errors than double differences if instrument errors are small. Double differences represent biases between two radiometers regardless of their differences in frequency, EIA and bandwidth. They are expected to be less sensitive to simulation errors than single differences because the subtraction of two single differences cancels out some uncertainties [*Yang*, 2016; *Yang and McKague*, 2016]. Thus looking at both single and double differences gives a sense of the magnitude of simulation biases and actual radiometer calibration biases. The over-ocean collocation method is the main intercalibration method and has been applied to a number of radiometers [*Wentz et al.*, 2001; *Yan and Weng*, 2008; *McKague et al.*, 2011; *John et al.*, 2012; *Biswas et al.*, 2013; *Sapiano et al.*, 2013; *Wilheit*, 2013; *Mo*, 2014; *Wilheit et al.*, 2015; *Yang et al.*, 2015; *Yang and McKague*, 2016]. It should be noted that there are other intercalibration methods [*Ruf*, 2000; *Yang et al.*, 2016b], which can produce different results.

A one dimensional plane-parallel RTM is used [*Yang et al.*, 2014; *Yang*, 2016; *Yang and McKague*, 2016; *Yang et al.*, 2016b]. The RTM is coded in a highly vectorized way to allow for fast parallel simulations for many (hundreds of thousands) FOVs with multiple frequencies and EIAs [*Yang*, 2016; *Yang and McKague*, 2016]. It includes atmospheric absorption models of Liebe and Rosenkranz modules from previous research with atmospheric absorption [*Liebe et al.*, 1991; *Liebe et al.*, 1992; *Rosenkranz*,

1993; 1998] and the Elsaesser surface emissivity model [*Hollinger*, 1971; *Stogryn*, 1972; *Wilheit*, 1979; *Elsaesser*, 2006]. The RTM is only for simulating clear-sky scenes. Before RTM simulation, precipitation and clouds are screened with empirical filters [*Stogryn et al.*, 1994] as shown in the appendix. The geophysical fields used, including surface and atmospheric parameters, are from the National Centers for Environmental Prediction (NCEP) Final (FNL) Tropospheric Analyses data, which are also commonly referred to as Global Data Assimilation System (GDAS). NCEP FNL data have 1°×1° horizontal resolution, 26 vertical layers, and 6-hour temporal resolution.

In this study, the radiometer GMI is intercalibrated to WindSat. GMI is a conical-scanning microwave radiometer onboard GPM core observatory [*Hou et al.*, 2014; *Draper et al.*, 2015a]. The spacecraft orbit has a 65° inclination with a mean altitude of 407 km and GMI's conical scanning extends observations to ±68° latitude. Its non sun-synchronous orbit allows Earth sampling that can capture precipitation diurnal variability. It is the reference radiometer to which all other GPM constellation radiometers are calibrated and has shown stable and accurate performance so far [*Hou et al.*, 2014; *Draper et al.*, 2015a; *Wilheit et al.*, 2015; *Wentz and Draper*, 2016]. GMI has 13 channels from 10 – 183 GHz with dual polarization (vertical and horizontal) at all but the 23 and 183 GHz channels. A number of calibration efforts have been performed to GMI and show its well performance [*Draper et al.*, 2015a; *Yang et al.*, 2015; *Yang and McKague*, 2016; *Yang et al.*, 2016b]. The noise-diode with GMI indicates no issues of radiometer nonlinearity [*Draper et al.*, 2015b]. Deep-space maneuver has been performed to calibrate GMI against the cosmic background [*Wentz and Draper*, 2016]. As the cosmic background is homogeneous with known temperature, it has been found very useful to examine radiometer and refine APC algorithm with deep-space maneuver [*Wentz et al.*, 2001; *Weng et al.*, 2013a; *Yang et al.*, 2016a]. WindSat is aboard the Coriolis

spacecraft, which was launched on January 6, 2003 into a sun-synchronous orbit with 98.7° inclination and 840 km mean altitude [*Gaiser et al.*, 2004]. It is a conical-scanning polarimetric microwave radiometer with 22 channels at five frequencies. The WindSat calibration indicates its stable performance [*Gaiser et al.*, 2004; *Jones et al.*, 2006; *Ruf et al.*, 2006; *Wilheit*, 2013].

In this study, the coincident channels between GMI (target radiometer) and WindSat (reference radiometer) are intercalibrated. Radiometer biases are estimated using single and double differences. These are the GMI 10.65 (V&H), 18.7 (V&H), 23.8V, and 36.64 (V&H) channels together with the WindSat 10.7 (V&H), 18.7 (V&H), 23.8V, and 37 (V&H) channels. The GMI data are archived and distributed by the NASA Precipitation Processing System (PPS) [*Precipitation Processing* System *(PPS)*, 2014]. A preliminary version of GMI version 4 Level-1C dataset referred to as ITE030 is used in this analysis. This version has the TB data with latest APC and a number of calibration corrections applied and is available in the current PPS GMI product [*Draper*, 2014; *Yang et al.*, 2015]. The GMI APC algorithm has been developed to convert raw count to TA and TB. The APC algorithm has been examined and refined with comprehensive efforts through prelaunch test, onboard calibration system, deep-space maneuver, and simulation [*Draper*, 2014; *Draper et al.*, 2015a; *Draper et al.*, 2015b; *Wentz and Draper*, 2016]. For instance, results based on the deep-space maneuver estimate an accuracy of 0.1 K for TA and 0.25 K for TB [*Wentz and Draper*, 2016]. Problems such as the along-scan biases in warm scenes have been identified in early GMI data versions and subsequently corrected [*Yang et al.*, 2015]. WindSat data are version 2.0.0 of the Sensor Data Record (SDR) from the Naval Research Laboratory [*Gaiser et al.*, 2004]. The SDR data of WindSat are equivalent to the Level-1 TB data of GMI in terms of the data layout. One year's data from 4 March 2014 to 30 April 2015 are used.

The data of other GPM radiometers have also been studied to verify our findings. These radiometers are Tropical Rainfall Measuring Mission's (TRMM) Microwave Imager (TMI), Special Sensor Microwave Imager/Sounder (SSMIS) (F16 - F18), Advanced Microwave Scanning Radiometer 2 (AMSR2). The brightness temperature data of Level-1B (not intercalibrated) from PPS are used. The same intercalibration methodology as aforementioned is applied to these radiometers. A total of seven radiometers and eleven pairing combinations with intercalibration have been performed. The results confirm the findings of intercalibration variability and non-monotonic features. The variability can be explained by our proposed model. For the sake of brevity, a summary of those results is presented in Section 3.

3. Calibration variability

3.1 Collocation oscillation dependence on spacecraft orbits

Collocation-based intercalibration is dependent on spacecraft orbit variations. Spacecraft orbits determine the location of collocation regions, which can change periodically. An example is shown in Figure 1. The collocations of two consecutive orbits of GMI and WindSat are shown. The orbit ground tracks (spacecraft nadir view) of GMI and WindSat shift westward. The collocations are in high-latitude regions on January 1st, 2015, shift to tropics after ~20 days on January 20th, and back to high-latitude regions ~20 days later.

Figure 2 shows details about the collocation change and periodicity. The one-year variability of GMI/WindSat collocation is shown in terms of latitude and longitude with the histogram shown in color. The latitude of the collocations changes periodically between high latitudes and the tropics, and appears as the superposition of two sinusoidal waves symmetric about the equator. The Fourier transform is

implemented and indicates that the period of oscillation is ~40 days. Variations in the longitude of the collocation exhibit the same periodic behavior as that of latitude. It is shown in the next section that changes in brightness temperature calibration biases have a similar temporal periodic behavior correlated to collocation oscillation.

An analytical orbit model to describe the source of these periodic variations is derived here. GMI and WindSat are in nearly circular low Earth orbits (LEO). Each orbit generally does not follow the exact same track as the previous orbit, but rather systematically shifts. This is due to two reasons: rotation of the Earth rotation and orbit precession. Orbit precession is mainly due to the fact that the Earth is not a perfect sphere, but rather is an oblate spheroid, which results in a non-uniform gravitational field. This results in orbit perturbations, with the dominant effect for a LEO spacecraft being an orbit nodal precession. The orbit nodes, the intersections between spacecraft orbits and the Earth's equator, precess at a relatively stable and predictable rate.

For two spacecrafts, the location of the intersections between their orbits changes. In particular, there is a latitudinal oscillation between high-latitude and tropical regions. This latitudinal dependence in turn effects the predominant values of geophysical parameters and TBs. The period of the oscillation is given by

$$T = \frac{L}{2\left|v_2 - v_1\right|} \tag{1}$$

where L is the longitudinal range of a complete orbit, which is 360° in the angular coordinates, v_1 and v_2 are the speed of movement for each spacecraft orbit, and the constant 2 is accounting for the fact that latitude oscillations are symmetric with respect to equator, which reduces the oscillation period by half. The speed of movement for each spacecraft orbit is

$$\begin{aligned} v_1 &= \alpha_E + \alpha_{p1} \\ v_2 &= \alpha_E + \alpha_{p2} \end{aligned} \tag{2}$$

where α_E is the Earth rotation rate (360 degree per day), and $\alpha_{p1,2}$ and α_{p1} are the precession rates for the two spacecrafts respectively. Combining Equations 1 and 2, the Earth rotation rate is cancelled out:

$$T = \frac{360}{2\left|\alpha_{p2} - \alpha_{p1}\right|} \tag{3}$$

The precession rate (in radians per second) is [*Griffin and French*, 2004]:

$$\alpha_p = -\frac{3}{2}\sqrt{\frac{GM}{a^3}} J_2 \left(\frac{R_E}{a}\right)^2 \frac{\cos i}{(1-e^2)^2} \tag{4}$$

where G is the gravitational constant, 6.67408×10^{-11} $m^3kg^{-1}s^{-2}$, M is the Earth mass, 5.972×10^{24} kg, J_2 is second zonal harmonic coefficient indicating the orbit perturbation due to Earth oblateness, 1.08263×10^{-3}, R_E is the Earth semi-major radius, 6378.137×10^3 m, a is the semi-major axis of the spacecraft orbit, which is given by the Earth radius plus the spacecraft altitude h ($a = R_E + h$), i is the orbit inclination angle, e is the orbit eccentricity, which is approximately zero for a typical LEO orbit. We see that the precession rate can be positive or negative depending on the inclination angle. Equation 4 can be simplified to produce the nodal precession rate in degrees per day as follows:

$$\alpha_p = -6.529\times10^{24} \frac{\cos i}{a^{3.5}} \tag{5}$$

Combining Equations 3 and 5, we obtain the oscillation period between two spacecraft orbits in units of days as:

$$T = \frac{360}{2 \times 6.529 \times 10^{24} \left| a_1^{-3.5} \cos i_1 - a_2^{-3.5} \cos i_2 \right|} \quad (6)$$

For instance, the orbit parameters are 407×10^3 m altitude and 65° inclination for GMI, and 840×10^3 m and 98.7° for WindSat. The oscillation period is 40 days according to the analytic calculation. In comparison, it is 41 days calculated from the observed collocation data. In fact, we have done intercalibration for a number of radiometers. Tables 1 and 2 list the orbit specifications and results of oscillation periods from both the analytic function and observational data. The analytic calculation agrees well with observations. Our model does not account for Earth roughness, ocean currents, ground water run-off and storage, etc., which change the gravitational field but are higher order factors compared to Earth oblateness. The spacecraft orbit is also affected by atmospheric drag, solar wind, radiation pressure, and other celestial bodies like the Moon, which can result in discrepancies between our model and observations.

3.2 Temporal variability

As the collocation oscillates with spacecraft orbit, intercalibration estimates from single and double differences are significantly affected. A variation in the intercalibration estimate is found by examining the time series of GMI/WindSat intercalibration. Figure 3 shows the calibration time series of single and double differences for GMI and WindSat as well as their corresponding power spectra. The power spectra show a clear signal with ~40 day period in both single and double differences. This 40 day signal is present in all channels. In general, H-polarization (H-pol) channels have stronger amplitude than V-pol; the water vapor channel 23.8V also has pronounced amplitude in its power spectrum. The results imply that the signal is related to a combination of water vapor and surface features. Some other signals with different periods are also noted, but with weaker amplitudes. In fact, the oscillation in intercalibration is always

present as we calibrate different radiometers. The oscillation is not negligible. The single and double differences are key variables to perform intercalibration as introduced in the Appendix. The ranges of oscillation at the seven channels are 3.3, 2.6, 3.5, 3.4, 3.7, 2.7, 4.1 K for single difference, and 1.0, 1.1, 1.7, 1.9, 1.8, 1.5, 1.7 K for double difference, respectively. The results are striking because the double difference is generally expected to be less sensitive to biases such as simulation errors compared to single difference. These are expected to cancel with the double difference process. We will discuss the error sources later.

Corresponding geophysical parameters are examined. Over the ocean, there are three major geophysical parameters affecting calibration through observations and the RTM - water vapor, surface wind speed (SWS), and sea surface temperature (SST). Therefore, these three parameters are investigated in terms of columnar water vapor mass (absolute humidity, g/m^2), SWS (m/s), and SST (Kelvins), which are drawn from the ancillary NCEP FNL data. The three geophysical parameters all have this 40 day signal as shown in Figure 4. The observed TB is also examined as it depends on these geophysical parameters. All channels have the 40 day signal, which is generally stronger in H-pol than V-pol. These results suggest a correlation between calibration variability and geophysical parameters.

To characterize the calibration variability, the calibration dependence on water vapor is examined from the 3D temporal variability perspective, as shown in Figure 5. The single and double differences are shown in the left and right columns, respectively. The single difference is for GMI (WindSat shows similar results as GMI). The mean of the single difference is subtracted for each channel. The red and blues ellipses highlight the positive and negative departures, respectively. Three different types of dependence are found, depending on the channel. The first type is the monotonic dependence, where single or double difference

shows monotonic increase or decrease with the change of water vapor. In channels 10.65V and 18.7V, single difference is large with low water vapor, but becomes smaller with high water vapor. Monotonic dependence occurs in channels 18.7H and 23.8V for double difference. The second type is non-monotonic. In channels 10.65H, 18.7H and 23.8V, single difference is large with low water vapor below 30 g/m^2, small with moderate water vapor between 30 and 80 g/m^2, and large again with high water vapor from 80 to 250 g/m^2. In this non-monotonic type, the single difference is extremely large with very high water vapor beyond 150 g/m^2. The third type is that the single or double difference does not show a significant dependence on water vapor. The three types can mix with each other. The dependence of the double difference on water vapor is reduced, compared to that of the single difference. However, a pronounced variability with a range of more than 1 K is seen at channels such as 18.7V, 18.7H and 23.8V. Temporal differences are found. For instance, channel 18.7V has noticeably larger double differences from March – July compared to later months.

SWS has a pronounced impact on both single and double differences. In Figure 6, single difference is found to have either monotonic increase or decrease with SWS, depending on the channel. For 10.65H, 18.7H and 36.64H, single difference monotonically increases with SWS; it decreases for 10.65V, 18.7V, 23.8V, 36.64V. Slightly non-monotonic dependence is noticed for 23.8V and 36.64V, where large single difference is observed with both very low (<5 m/s) and high (>15 m/s) SWS. The double difference becomes either very large (10.65V, 18.7H, 23.8V, 36.64V, 36.64H) or very small (18.7V) with SWS larger than 15 m/s. The impact of SWS persists with locations crossing both tropical and high-latitude regions. Channel 10.65V, for instance, keeps large single and double differences for high SWS (>15 m/s) throughout the time. Compared to water vapor, SWS demonstrates stronger impact on single difference.

For example, average single differences at 18.7V are 2.5K and -1.5K for high (>15 m/s) and low (<10 m/s) SWS respectively, differing by as much as 4 K. The impact from other geophysical parameters such as water vapor is noticeable, where the 40 day signal is pronounced with low SWS.

SST shows similar impact on calibration as water vapor, but with some differences worth noting. In Figure 7, the SST dependent temporal variability is shown for single and double differences, respectively. SST affects calibration and shows monotonic or non-monotonic dependence similar to that of water vapor. Since SST and water vapor are correlated in terms of temporal and spatial variability (Section IV), their impact on calibration is also correlated. On the other hand, SST shows less impact on calibration than water vapor and SWS, as shown in the more uniformly distributed color. For instance, while low water vapor (<5 m/s) tends to correspond to high single difference, low SST (<277 K) does not show much difference relative to moderate SST (277-280 K).

Calibration has a strong latitudinal dependence. Figure 8 show the latitudinal variability for single and double differences respectively. Calibration location shows a latitudinal oscillation with a 40 day period. A pronounced high single difference is observed in the tropics for channels 10.65H, 18.7H, and 23.8V. This is consistent with the previous temporal variability analysis, where high geophysical parameters result in either high or low single difference. For channels 10.65V, a high single difference is observed at high latitudes, agreeing with the SWS temporal analysis. The double difference is smaller in tropics than high latitude for 18.7H and 23.8V, opposite to that of single difference. Channel 18.7V has a larger double difference in the first five months, as confirmed in previous analysis. Although not shown here, the longitudinal impact is also found but with weaker amplitude than that of latitude.

3.3 Spatial variability

Calibration's spatial variability determines its temporal variability. Figure 9 shows the spatial distribution for collocation and geophysical parameters. More collocations occur at high latitude (~±60º), since the GMI orbit places it in these latitudes more often over a given time period. Water vapor is abundant in the tropics. It also has longitudinal variability such that more water vapor is present in the West Pacific than in the East Pacific. Likewise, SST also shows regional differences, but with less variability than water vapor. SWS is higher in high latitude zones (~±50º) and is stronger in southern hemisphere where land areas are smaller. Longitudinally, SWS is higher in the East Pacific than in the West Pacific (opposite to water vapor and SST).

The intercalibration regional dependence is found. In Figure 10, most channels show larger single difference in the tropics, except for channel 10.65V with lower single difference in tropics. Longitudinal variability is also present. For example, single difference is larger in the West Pacific than East Pacific. The double difference in channels 18.7H and 23.8V is smaller in tropics, opposite to that of single difference. Longitudinally, the two channels also flip with colder double difference in the West Pacific than East Pacific. These spatial patterns resemble geophysical parameters, particularly water vapor and SWS. Noticeable negative departure of double differences at 10V and 10H is seen near coastal regions such as Europe, West Africa and America. This is due to the large FOVs of WindSat, which result in land contamination and large single differences. Although a 1°×1° land-sea mask is used to screen out land scenes, land scenes cannot be fully eliminated due to this resolution limitation. Relatively warm land contamination results in large positive single differences for WindSat and therefore negative double differences for GMI relative to WindSat.

The calibration spatial variability confirms its dependence on geophysical parameters and correlates to temporal variability. The collocation depends on spacecraft orbits. Due to spatial variability, the collocation oscillation leads to temporal variability. One important implication is that calibration at a limited local region can have biases. For instance, spacecraft of low Earth inclination sees mostly tropical regions with corresponding biases depending on the channel. Even for a polar orbit spacecraft, the conditional sampling can also bias calibration since it is not uniformly weighted over the Earth. These biases are rooted in a combination of sources between the RTM, ancillary geophysical data, and potentially the calibration of the radiometers themselves.

4. Calibration dependence on geophysical parameters and TB

The calibration dependence on geophysical parameters and TB is considered. Figure 11 shows the number density plots of calibration dependence on water vapor. The left and right columns are for single and double differences, respectively. The mean and standard deviation (mean plus and minus mean) are denoted in solid and dashed lines, respectively. All channels show that modeling overall underestimates observations, particularly with high water vapor conditions. Nonlinearity is seen in all channels. A left-side tilt-up tail is present with low water vapor (<40 g/m2). A slight bump with middle-range water vapor (100-160 g/m2) is seen, particularly at 23.8V. The single difference increases with high water vapor (>160 g/m2). The nonlinearity for double difference is reduced compared to single difference. However, residual nonlinearity is seen with low water vapor. The overall dependence of double difference on water vapor becomes negative, contrast to the positive slope in single difference. The maximum standard deviations are significant with 3.1 and 2.0 K at 36.6H for single and double differences, respectively. The nonlinearity and

large uncertainties are issues that are not typically addressed with current calibration methods. The non-monotonicity occurs in a relatively narrow dynamic range of TB with solely cold ocean scenes.

Likewise, the dependence on SWS is shown in Figure 12. The pronounced nonlinear and non-monotonic dependence is found. The V-pol channels bends with SWS ~7m/s, tilts up towards both ends, and drops with SWS larger than 18 m/s. The H-pol channels also shows nonlinearity with an overall negative dependence on SWS. The magnitude of nonlinearity and non-monotonicity is reduced but still appreciable for double difference. The overall dependence flips from negative to positive for channels 18.7V&H, 23.8V, and 36.64H, relative to single difference. The uncertainties are larger than that of water vapor with maximum standard deviations of 3.7 and 2.9 K for single and double differences respectively. Wind speed is a major factor affecting calibration through parameterization in the emissivity model. For window channels, the surface emission dominates. The emissivity dependence on TB and frequency is empirically parameterized in model [*Elsaesser*, 2006]. Errors due to inaccurate parameterization can result in nonlinear and non-monotonic discrepancies as found here.

Figure 13 shows the results for SST. SST appears to have two modes with a number of samples at cold (270-277ºC) and warm (300-305ºC) SSTs. Single differences tilt up at warm TBs. In channel 18.7H, single differences increase significantly for SST larger than 285 K. A positive dependence is seen at all channels. The H-pol channels show more significant scattering than V-pol. For double differences, channels 18.7H and 23.8V show negative dependence, opposite to that of single differences.

The calibration dependence on TB is examined in Figure 14. Since TB is a function of all three geophysical parameters, the TB dependence shows combined features from all geophysical parameters. For

instance, channel 10.65V has a bi-modal feature as with SST. The V-pol channels tilt up at low to moderate TBs, which represent the water vapor features. Channel 10.65H shows an oscillating feature like SWS. A positive dependence on TB is observed in single differences but becomes negative at some channels for double differences. The maximum standard deviations are significant with 3.2 and 2.0 K for single and double differences respectively. Overall, the combination of all three geophysical parameters makes the calibration uncertainties more complicated and difficult to remove. Although not shown here, the non-monotonic features are also found in all seven radiometers with eleven combinations as listed in Tables 1 and 2.

5. Discussion and Conclusion

Intercalibration is a fundamental process for integrating radiometer constellation data. The intercalibration stability estimate shows ubiquitous temporal and spatial variability and nonlinear and non-monotonic errors dependent on geophysical parameters. A periodic time oscillation is found with intercalibration biases for all radiometer channels. The oscillation is significant with ranges as large as 4 and 2 K for single and double differences respectively. The signal is due to the oscillation of the collocation of the intercalibrated radiometers as a function of their orbit. An analytic orbit model is derived and can reproduce the collocation periodicity. Calibration shows spatial variability due to the regional difference of geophysical parameters. The spatial variability is a function of both latitude and longitude and is channel dependent. The temporal and spatial variability is correlated through the orbit dependent sampling. Since the study is based on the over-ocean collocation method, results such as the specific periodicity of temporal variability can differ from other calibration methods. But features like spatial variability are expected to be

similar as discussed below. But features like spatial variability are expected to be similar as discussed below.

Nonlinear and non-monotonic uncertainties are found in intercalibration and are dependent on geophysical parameters. The nonlinearity and non-monotonicity result in uncertainties as large as 3.7 and 2.9 K in term of standard deviation for single and double differences respectively, which cannot be removed by simple linear regression. These nonlinear and non-monotonic dependences are more sensitive to water vapor and SWS than SST. The dependence of calibration on TB becomes more complex due to the combination of all geophysical parameters. These uncertainties occur not only with large values of geophysical parameters, but also with small values under calm weather conditions. Since calm weather conditions are commonly used for calibration, the uncertainties should be noted and addressed in future studies.

Factors including instrument issues and RTM simulation errors can affect the intercalibration uncertainties. These factors can mingle together and complicate the problem. Deconvolving different factors and resolving the problem require extensive efforts covering prelaunch test, in-flight data, APC analysis, deep-space maneuver, simulation, and assimilation data comparison, etc. This work alone cannot resolve the complicated issues, however it sheds light on the problem. Seven microwave radiometers with eleven combinations are studied. Oscillation and non-monotonic features of intercalibration uncertainties are found with all of the eleven combinations. The oscillation periods and magnitudes are dependent on the specific radiometer pairing. Instrument issues alone (e.g. nonlinearity) are difficult to explain the ubiquitous oscillation with varying periods and magnitudes dependent on radiometer pairing and the non-monotonic features. The periods of the observed oscillations are consistent with the orbital characteristics

of the intercalibration pairs. On the other hand, instrument issues cannot be excluded with this study alone and more investigations such as APC algorithm, inflight performance, and spacecraft maneuvers should be conducted. Since the regional dependence of intercalibration uncertainties and its non-monotonic features are observed, future investigations would be worthwhile to examine whether they can be mitigated with different RTMs and ancillary geophysical data. For example, while NCEP FNL data are used in simulations in this study, uncertainties with the reanalysis data have been noted that can bias the simulations [*Bengtsson et al.*, 2007; *Kleist et al.*, 2009]. Alternative ancillary data such as different reanalysis data [*Geer et al.*, 2010], GPS occultation [*Weng et al.,* 2013b; *Zou et al.,* 2014], and radiosonde [*Moradi et al.,* 2010] can be applied for comparison. As there are a variety of RTMs with different surface emissivity models and atmospheric absorption models, a comprehensive comparison between different RTMs can help quantify the uncertainties with simulations. Intercalibration uncertainties can be better understood by investigating error budgets in both instrument and simulation.

We suggest techniques to mitigate these calibration issues before they are fully resolved. Appropriate conditional sampling should be performed. The conditional sampling of spacecraft collocation has spatial and temporal variability with a predictable periodicity. Biases can be produced when averaging incomplete cycles. An integer number of cycles should be used and the length of the cycle can be determined for any two instruments with our orbit model. Large biases can be produced for spacecraft with different inclination angles, which cover different latitudinal zones. Constraining data to the same latitudinal and longitudinal areas can reduce these biases.

Appendix

The radiometer observed TB can be simulated as [*Yang and McKague*, 2016; *Yang et al.*, 2016b]:

$$\mathrm{TB} = \varepsilon T \exp(-\tau \sec\theta) + \mathrm{TB}_{\mathrm{up}} + (1-\varepsilon)\exp(-\tau \sec\theta)\mathrm{TB}_{\mathrm{dn}} + (1-\varepsilon)\mathrm{TB}_{\mathrm{cos}} \exp(-2\tau \sec\theta) \quad (1)$$

where T is the sea surface temperature, ε is the surface emissivity, τ is the vertical atmospheric optical depth, θ is the EIA, $\mathrm{TB}_{\mathrm{up}}$ and $\mathrm{TB}_{\mathrm{dn}}$ are atmospheric upwelling and downwelling emission respectively, and $\mathrm{TB}_{\mathrm{cos}}$ is the cosmic background.

The atmospheric emission terms at a given frequency, $\mathrm{TB}_{\mathrm{up}}$ and $\mathrm{TB}_{\mathrm{dn}}$, are calculated as

$$\mathrm{TB}_{\mathrm{up}} = \int_0^{TOA} T(z)\alpha(z)\sec\theta \exp(-\int_{z'}^{TOA} \sec\theta\alpha(z')dz')dz \quad (2)$$
$$\mathrm{TB}_{\mathrm{dn}} = \int_{TOA}^{0} T(z)\alpha(z)\sec\theta \exp(-\int_{TOA}^{z} \sec\theta\alpha(z')dz')dz$$

where z is the vertical height, α is the atmospheric absorption profile, *TOA* is top of atmosphere.

The definition of single difference is

$$\mathrm{SD} = \mathrm{TB}_{\mathrm{obs}} - \mathrm{TB}_{sim} \quad (3)$$

where $\mathrm{TB}_{\mathrm{obs}}$ is the observed TB and $\mathrm{TB}_{\mathrm{sim}}$ is the simulated TB.

The definition of double difference is

$$\mathrm{DD} = \mathrm{SD}_{\mathrm{target}} - SD_{reference} \quad (4)$$

where $\mathrm{SD}_{\mathrm{target}}$ and $\mathrm{SD}_{\mathrm{reference}}$ are single differences for the target and reference radiometers, respectively. The double difference accounts for instrument difference in frequency and EIA and is generally believed to be insensitive to modeling uncertainties.

Empirical filters are used to screen out the precipitation and heavy clouds before simulation [*Stogryn et al.*, 1994]

$$\begin{aligned} &TB_{37V}\text{-}TB_{37H} > 50K \\ &TB_{19V} < TB_{37V} \\ &TB_{19H} < 185K \\ &TB_{37H} < 210K \end{aligned} \quad (5)$$

Acknowledgment

This work has been partially supported by a grant from NASA. The GMI data are available from NASA Precipitation Measurement Missions (PMM) (http://pps.gsfc.nasa.gov/). The WindSat data are available from the FTP site (arthurhou.pps.eosdis.nasa.gov). The NCEP FNL data are from the University Corporation for Atmospheric Research (UCAR) (http://rda.ucar.edu/)

Figure and Table Captions

Figure 1. The collocations from consecutive two orbits of GMI (green) and WindSat (red) on (top) Jan 1st, (middle) Jan 20th, and (bottom) Feb 10th, 2015. The collocations move first from high-latitude to tropics and then back to high-latitude again.

Figure 2. Time series of collocation latitude (top) and longitude (bottom) for GMI and WindSat. A signal with a ~40 day period is found in both single and double differences at all channels.

Figure 3. Time series (left) of single difference (GMI) and double difference (GMI/WindSat) and corresponding power spectra (right). A signal with a ~40 day period is found in both single and double differences at all channels with pronounced magnitudes (maximum peak-to-peak values are 4 and 2 K for single and double differences respectively)

Figure 4. Time series of geophysical parameters (water vapor, SWS, and SST) and TB. The 40 day signal is

also found.

Figure 5. The temporal variability of water vapor dependent single (GMI) and double difference (GMI/WindSat). The positive and negative departures are highlighted, showing different types of dependence with different channels. Single difference shows monotonic negative dependence on water vapor in channel 10.65Vand 18.7V, non-monotonic dependence in 10.65H, 18.7H and 23.8V, and relatively neutral in 36.64V&H. Double difference can have opposite monotonicity as single difference.

Figure 6. The temporal variability of SWS dependent single (GMI) and double difference (GMI/WindSat) with highlighted positive or negative departures. SWS also has a significant impact on calibration with monotonic or non-monotonic features.

Figure 7. The temporal variability of SST dependent single (GMI) and double difference (GMI/WindSat) with highlighted positive or negative departures.

Figure 8. The temporal variability of latitude dependent single (GMI) and double difference (GMI/WindSat) with highlighted positive or negative departures. The latitudinal dependence is significant. It is consistent with temporal variability and can be opposite between single and double differences.

Figure 9. The maps of collocation number, water vapor, SWS and SST. The geophysical parameters have pronounced regional dependence and affect calibration.

Figure 10. The maps of single (GMI) and double difference (GMI/WindSat). The positive and negative departures are highlighted and show latitudinal and longitudinal dependence. The spatial variability resembles that of geophysical parameters particularly water vapor and SWS. The noticeable negative departure of double difference at 10V and 10H is seen near coastal regions such as Europe, West America

and East America, which is due to the large FOVs of WindSat that result in land contamination and large WindSat single difference.

Figure 11. The dependence of single (GMI) and double difference (GMI/WindSat) on water vapor. The solid and dash lines show mean and standard deviation (plus and minus) with maximum standard deviations 3.1 and 2.0 K at 36.6H. Nonlinear and non-monotonic dependence is found with bump in the middle and drops at both ends.

Figure 12. The dependence of single (GMI) and double difference (GMI/WindSat) on SWS. Nonlinear and non-monotonic dependence is noticeable. The single differences in V-pol and H-pol channels show overall opposite trends that are positive and negative respectively. The uncertainties are larger than that of water vapor with maximum standard deviations of 3.7 and 2.9 K for single and double differences respectively.

Figure 13. The same as Figure 12 but for SST. SST has two modes with a number of samples at cold (270-277ºC) and warm (300-305ºC) SSTs. The nonlinearity and non-monotonicity are noticeable but smaller than that of water vapor and SWS.

Figure 14. The single (GMI) and double difference (GMI/WindSat) as a function of TB. Since TB is a function of all geophysical parameters, the nonlinearity and non-monotonicity are more significant (maximum standard deviations are 3.1 and 2.0 K for single and double differences respectively) with mixing features from geophysical parameters.

Table 1. Orbit altitudes and inclinations of different radiometers

Table 2. Oscillation periods (orbital model and observation) and magnitudes of TB (GMI/TMI) and DD that are the maximum peak-to-peak magnitudes of oscillation among intercalibrated channels.

References

Bengtsson, L., et al. (2007), The need for a dynamical climate reanalysis, *Bull. Amer. Meteorol. Soc.*, *88*(4), 495-501, doi:10.1175/bams-88-4-495.

Berg, W., R. P. S. Mathew, H. Jennifer, and K. Christian (2012), Improved Geolocation and Earth Incidence Angle Information for a Fundamental Climate Data Record of the SSM/I Sensors, *IEEE Transactions on Geoscience and Remote Sensing*, -1688.

Biswas, S. K., S. Farrar, K. Gopalan, A. Santos-Garcia, W. L. Jones, and S. Bilanow (2013), Intercalibration of Microwave Radiometer Brightness Temperatures for the Global Precipitation Measurement Mission, *IEEE Transactions on Geoscience and Remote Sensing*, *51*(3), 1465-1477, doi:10.1109/tgrs.2012.2217148.

Biswas, S. K., K. Gopalan, W. L. Jones, and S. Bilanow (2010), Correction of Time-Varying Radiometric Errors in TRMM Microwave Imager Calibrated Brightness Temperature Products, *IEEE Geoscience and Remote Sensing Letters*, *7*(4), 851-855, doi:10.1109/lgrs.2010.2050135.

Draper, D. W. (2014), Calibration Data Book for Global Precipitation Measurement (GPM) Microwave Imager (GMI), edited, p. 211, Ball Aerospace & Technologies Corp.

Draper, D. W., D. Newell, F. Wentz, S. Krimchansky, and G. Skofronick-Jackson (2015a), The Global Precipitation Measurement (GPM) Microwave Imager (GMI): Instrument Overview and Early On-Orbit Performance, *Selected Topics in Applied Earth Observations and Remote Sensing, IEEE Journal of*, *PP*(99), 1-11, doi:10.1109/JSTARS.2015.2403303.

Draper, D. W., D. A. Newell, D. S. McKague, and J. R. Piepmeier (2015b), Assessing Calibration Stability Using the Global Precipitation Measurement (GPM) Microwave Imager (GMI) Noise Diodes, *IEEE Journal of Selected Topics in Applied Earth Observations and Remote Sensing*, *8*(9), 4239-4247, doi:10.1109/jstars.2015.2406661.

Elsaesser, G. (2006), A parametric optimal estimation retrieval of the nonprecipitating parameters over the global oceans, M.S. Thesis, Colorado State Univ., Fort Collins, CO.

Gaiser, P. W., et al. (2004), The WindSat spaceborne polarimetric microwave radiometer: Sensor description and early orbit performance, *IEEE Transactions on Geoscience and Remote Sensing*, *42*(11), 2347-2361, doi:10.1109/tgrs.2004.836867.

Geer, A. J., P. Bauer, and N. Bormann (2010), Solar Biases in Microwave Imager Observations Assimilated at ECMWF, *IEEE Transactions on Geoscience and Remote Sensing*, *48*(6), 2660-2669, doi:10.1109/TGRS.2010.2040186.

Griffin, M., and J. French (2004), *Space Vehicle Design*, AIAA (American Institute of Aeronautics & Ast) Second Edition.

Hollinger, J. P. (1971), Passive microwave measurements of sea surface roughness, *Ieee Transactions on Geoscience Electronics*, *9*(3), 165-169, doi:10.1109/tge.1971.271489.

Hou, A. Y., R. K. Kakar, S. Neeck, A. A. Azarbarzin, C. D. Kummerow, M. Kojima, R. Oki, K. Nakamura, and T. Iguchi (2014), The global precipitation measurement mission, *Bull. Amer. Meteorol. Soc.*, *95*(5), 701-722, doi:10.1175/bams-d-13-00164.1.

John, V. O., G. Holl, S. A. Buehler, B. Candy, R. W. Saunders, and D. E. Parker (2012), Understanding intersatellite biases of microwave humidity sounders using global simultaneous nadir overpasses, *Journal of Geophysical Research-Atmospheres*, *117*, doi:10.1029/2011jd016349.

Jones, W. L., J. D. Park, S. Soisuvarn, L. Hong, P. W. Gaiser, and K. M. S. Germain (2006), Deep-space calibration of the WindSat radiometer, *IEEE Transactions on Geoscience and Remote Sensing*, *44*(3), 476-495, doi:10.1109/tgrs.2005.862499.

Joo, S., J. Eyre, and R. Marriott (2013), The Impact of MetOp and Other Satellite Data within the Met Office Global NWP System Using an Adjoint-Based Sensitivity Method, *Monthly Weather Review*, *141*(10), 3331-3342, doi:10.1175/mwr-d-12-00232.1.

Kleist, D. T., D. F. Parrish, J. C. Derber, R. Treadon, W. S. Wu, and S. Lord (2009), Introduction of the GSI into the NCEP Global Data Assimilation System, *Weather and Forecasting*, *24*(6), 1691-1705, doi:10.1175/2009waf2222201.1.

Liebe, H. J., G. A. Hufford, and T. Manabe (1991), A model for the complex permittivity of water at frequencies below 1 THz, *International Journal of Infrared and Millimeter Waves*, *12*(7), 659-675, doi:10.1007/bf01008897.

Liebe, H. J., P. W. Rosenkranz, and G. A. Hufford (1992), Atmospheric 60-GHz oxygen spectrum: New laboratory measurements and line parameters, *Journal of Quantitative Spectroscopy & Radiative Transfer*, *48*(5-6), 629-643, doi:10.1016/0022-4073(92)90127-p.

Lorenc, A. C., and R. T. Marriott (2014), Forecast sensitivity to observations in the Met Office Global numerical weather prediction system, *Quarterly Journal of the Royal Meteorological Society*, *140*(678), 209-224, doi:10.1002/qj.2122.

McKague, D. S., C. S. Ruf, and J. J. Puckett (2011), Beam Spoiling Correction for Spaceborne Microwave Radiometers Using the Two-Point Vicarious Calibration Method, *IEEE Transactions on Geoscience and Remote Sensing*, *49*(1), 21-27, doi:10.1109/tgrs.2010.2068052.

Meissner, T., and F. J. Wentz (2012), The Emissivity of the Ocean Surface Between 6 and 90 GHz Over a Large Range of Wind Speeds and Earth Incidence Angles, *IEEE Transactions on Geoscience and Remote Sensing*, *50*(8), 3004-3026, doi:10.1109/tgrs.2011.2179662.

Mo, T. (2010), Postlaunch calibration of the NOAA-19 Advanced Microwave Sounding Unit-A, *Journal of Geophysical Research-Atmospheres*, *115*, doi:10.1029/2009jd013177.

Mo, T. (2014), Inter-satellite calibration of the NOAA AMSU-A measurements over tropical oceans, *Remote Sens. Environ.*, *149*, 205-212, doi:10.1016/j.rse.2014.04.009.

Moradi, I., S. A. Buehler, and V. O. John (2010), Comparing upper tropospheric humidity from microwave satellite instruments and IGRA radiosonde data, paper presented at Microwave Radiometry and Remote Sensing of the Environment (MicroRad), 2010 11th Specialist Meeting on, 1-4 March 2010.

Payne, V. H., E. J. Mlawer, K. E. Cady-Pereira, and J. L. Moncet (2011), Water Vapor Continuum Absorption in the Microwave, *IEEE Transactions on Geoscience and Remote Sensing*, *49*(6), 2194-2208, doi:10.1109/tgrs.2010.2091416.

Precipitation Processing System (PPS) (2014), Algorithm Theoretical Basis Document (ATBD), NASA Global Precipitation Measurement (GPM) Level 1C Algorithms, Version 1.3, edited, p. 211, NASA GSFC.

Qin, Z., X. Zou, and F. Weng (2013), Analysis of ATMS striping noise from its Earth scene observations, *Journal of Geophysical Research: Atmospheres*, *118*(23), 2013JD020399, doi:10.1002/2013JD020399.

Rosenkranz, P. W. (1993), Absorption of microwaves by atmospheric gases, in *Atmospheric Remote Sensing by Microwave Radiometry*, edited by M. A. Janssen, pp. 37-90, John Wiley, New York.

Rosenkranz, P. W. (1998), Water vapor microwave continuum absorption: A comparison of measurements and models, *Radio Science*, *33*(4), 919-928, doi:10.1029/98rs01182.
Ruf, C. S. (2000), Detection of calibration drifts in spaceborne microwave radiometers using a vicarious cold reference, *IEEE Transactions on Geoscience and Remote Sensing*, *38*(1), 44-52, doi:10.1109/36.823900.
Ruf, C. S., Y. Hu, and S. T. Brown (2006), Calibration of WindSat polarimetric channels with a vicarious cold reference, *IEEE Transactions on Geoscience and Remote Sensing*, *44*(3), 470-475, doi:10.1109/tgrs.2005.855996.
Sapiano, M. R. P., W. K. Berg, D. S. McKague, and C. D. Kummerow (2013), Toward an Intercalibrated Fundamental Climate Data Record of the SSM/I Sensors, *IEEE Transactions on Geoscience and Remote Sensing*, *51*(3), 1492-1503, doi:10.1109/tgrs.2012.2206601.
Stogryn, A. P. (1972), The emissivity of sea foam at microwave frequencies, *Journal of Geophysical Research*, *77*(9), 1658-1666, doi:10.1029/JC077i009p01658.
Stogryn, A. P., C. T. Butler, and T. J. Bartolac (1994), Ocean surface wind retrievals from special sensor microwave imager data with neural networks, *Journal of Geophysical Research: Oceans*, *99*(C1), 981-984, doi:10.1029/93jc03042.
Ulaby, F. T., and D. G. Long (2014), *Microwave Radar and Radiometric Remote Sensing*, 1016 pp., Univ. of Michigan Press, ISBN 978-0-472-11935-6, Ann Arbor, MI.
Weng, F., H. Yang, and X. Zou (2013a), On Convertibility From Antenna to Sensor Brightness Temperature for ATMS, *IEEE Geoscience and Remote Sensing Letters*, *10*(4), 771-775, doi:10.1109/LGRS.2012.2223193.
Weng, F., X. Zou, N. Sun, H. Yang, M. Tian, W. J. Blackwell, X. Wang, L. Lin, and K. Anderson (2013b), Calibration of Suomi national polar-orbiting partnership advanced technology microwave sounder, *Journal of Geophysical Research-Atmospheres*, *118*(19), 11187-11200, doi:10.1002/jgrd.50840.
Wentz, F. J., P. Ashcroft, and C. Gentemann (2001), Post-launch calibration of the TRMM microwave imager, *IEEE Transactions on Geoscience and Remote Sensing*, *39*(2), 415-422, doi:10.1109/36.905249.
Wentz, F. J., and D. Draper (2016), On-Orbit Absolute Calibration of the Global Precipitation Measurement Microwave Imager, *Journal of Atmospheric and Oceanic Technology*, *33*(7), 1393-1412, doi:doi:10.1175/JTECH-D-15-0212.1.
Wilheit, T. T. (1979), A model for the microwave emissivity of the ocean's surface as a function of wind speed, *IEEE Transactions on Geoscience and Remote Sensing*, *17*(4), 244-249, doi:10.1109/tge.1979.294653.
Wilheit, T. T. (2013), Comparing Calibrations of Similar Conically Scanning Window-Channel Microwave Radiometers, *IEEE Transactions on Geoscience and Remote Sensing*, *51*(3), 1453-1464, doi:10.1109/tgrs.2012.2207122.
Wilheit, T. T., W. Berg, H. Ebrahimi, R. Kroodsma, D. McKague, V. Payne, and W. J. (2015), Intercalibrating the GPM constellation using the GPM microwave imager (GMI), *2015 IEEE International Geoscience and Remote Sensing Symposium (IGARSS)*.
Yan, B., and F. Weng (2008), Intercalibration between special sensor microwave imager/sounder and special sensor microwave imager, *IEEE Transactions on Geoscience and Remote Sensing*, *46*(4), 984-995, doi:10.1109/tgrs.2008.915752.
Yang, H., F. Weng, and K. Anderson (2016a), Estimation of ATMS Antenna Emission From Cold Space Observations, *IEEE Transactions on Geoscience and Remote Sensing*, *54*(8), 4479-4487, doi:10.1109/TGRS.2016.2542526.
Yang, J. X. (2016), Spaceborne Microwave Radiometry: Calibration, Intercalibration, and Science Applications, Doctoral Thesis, Univ. of Michigan, Ann Arbor, MI.
Yang, J. X., and D. S. McKague (2016), Improving Collocation-Based Scan-Dependent Intercalibration Over the Ocean for Spaceborne Radiometry, *IEEE Geoscience and Remote Sensing Letters*, *13*(4), 589-593.
Yang, J. X., D. S. McKague, and C. S. Ruf (2014), Land Contamination Correction for Passive Microwave Radiometer Data: Demonstration of Wind Retrieval in the Great Lakes Using SSM/I, *Journal of Atmospheric and Oceanic Technology*, *31*(10), 2094-2113, doi:10.1175/jtech-d-13-00254.1.
Yang, J. X., D. S. McKague, and C. S. Ruf (2015), Identifying and resolving a calibration issue with GMI, *2015 IEEE International Geoscience and Remote Sensing Symposium (IGARSS)*, 2568-2571.
Yang, J. X., D. S. McKague, and C. S. Ruf (2016b), Boreal, Temperate, and Tropical Forests as Vicarious Calibration Sites for Spaceborne Microwave Radiometry, *IEEE Transactions on Geoscience and Remote Sensing*, *54*(2), 1035-1051.
Zou, X., L. Lin, and F. Weng (2014), Absolute Calibration of ATMS Upper Level Temperature Sounding Channels Using GPS RO Observations, *IEEE Transactions on Geoscience and Remote Sensing*, *52*(2), 1397-1406, doi:10.1109/TGRS.2013.2250981.

Lists of Tables

Table 1. Orbit altitudes and inclinations of different radiometers

Instrument	Orbit Altitude (km)	Orbit Inclination (degree)
GMI	407	65
AMSR2	700	98.2
TMI	403	35
WindSat	840	98.7
SSMIS F16	853	98.9
SSMIS F17	853	98.9
SSMIS F18	853	98.9

Table 2. Oscillation periods (orbital model and observation) and magnitudes of TB (GMI/TMI) and DD that are the maximum peak-to-peak magnitudes of oscillation among intercalibrated channels.

Instrument Pair	Oscillation Period from Model (day)	Oscillation Period from Observation (day)	Maximum Magnitude of GMI/TMI TB Oscillation (K)	Maximum Magnitude of DD Oscillation (K)
GMI-AMSR2	40	41	61@89H	1.5@89H
GMI-F16	40	41	58@89H	1.6@89H
GMI-F17	40	41	64@89H	1.7@89H
GMI-F18	40	41	62@89H	1.7@89H
GMI-TMI	52	56	49@89H	1.8@89H

GMI/WindSat	40	41	62@23.8V	1.9@23.8V
TMI/WindSat	24	23	53@21V	2.1@21V
TMI/AMSR2	24	24	54@85.5H	2@85.5H
TMI/F16	24	24	52@85.5H	2@85.5H
TMI/F17	24	24	55@85.5H	2.1@85.5H
TMI/F18	24	24	53@85.5H	2@85.5H

Lists of Figures

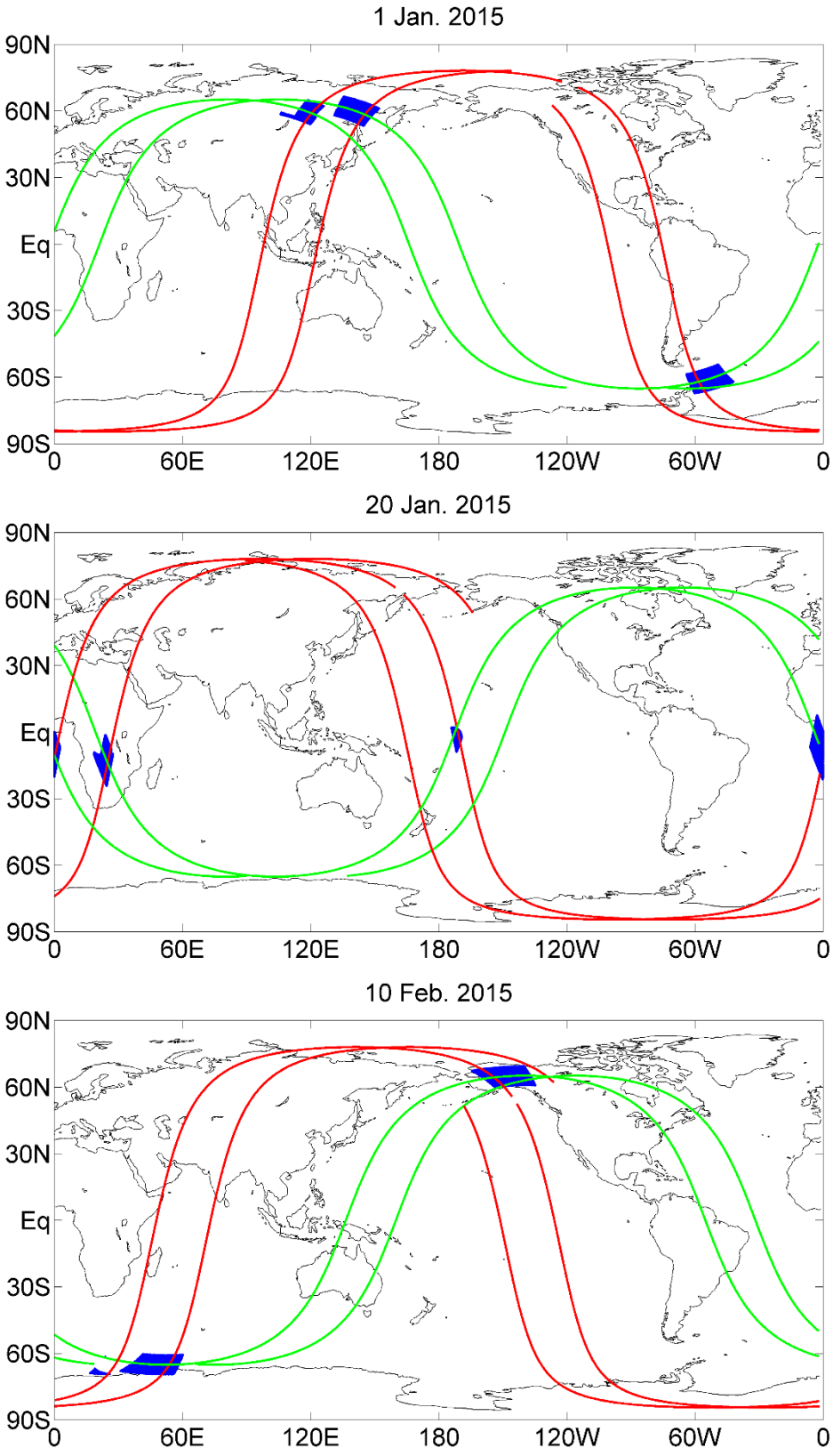

Figure 1. The collocations from consecutive two orbits of GMI (green) and WindSat (red) on (top) Jan 1st, (middle) Jan 20th, and (bottom) Feb 10th, 2015. The collocations move first from high-latitude to tropics and then back to high-latitude again.

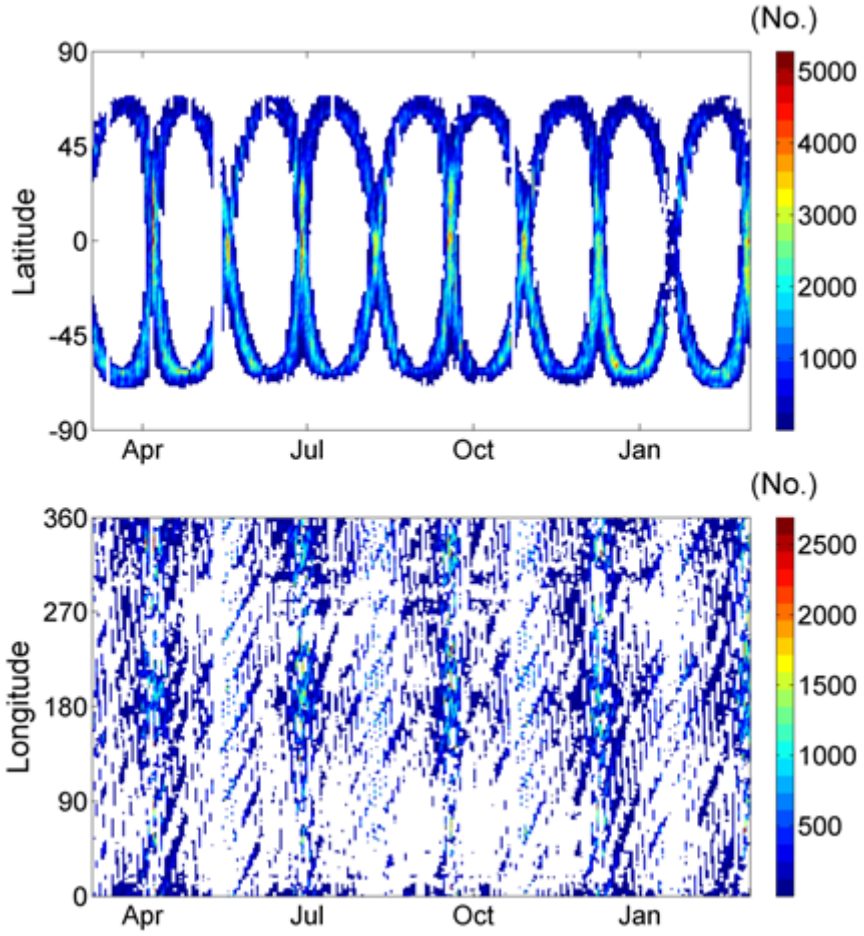

Figure 2. Time series of collocation latitude (top) and longitude (bottom) for GMI and WindSat. A signal with a ~40 day period is found in both single and double differences at all channels.

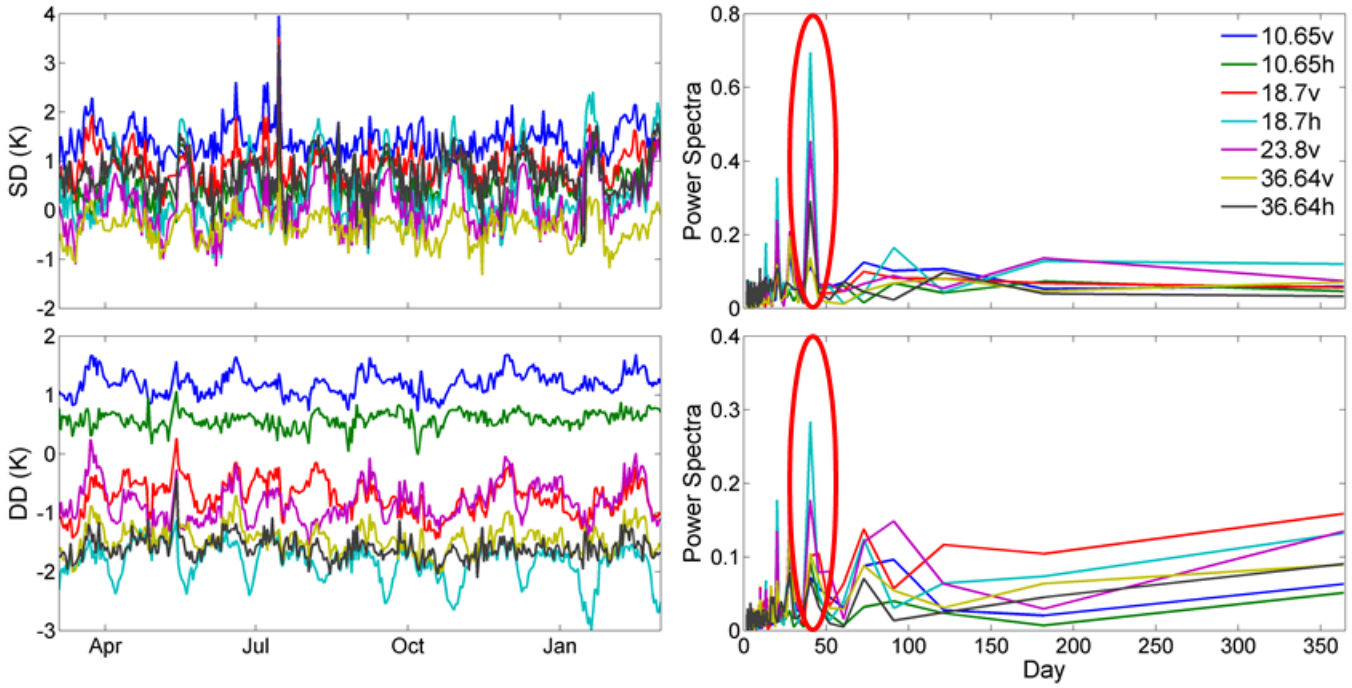

Figure 3. Time series (left) of single difference (GMI) and double difference (GMI/WindSat) and corresponding power spectra (right). A signal with a ~40 day period is found in both single and double differences at all channels with pronounced magnitudes (maximum peak-to-peak values are 4 and 2 K for single and double differences respectively)

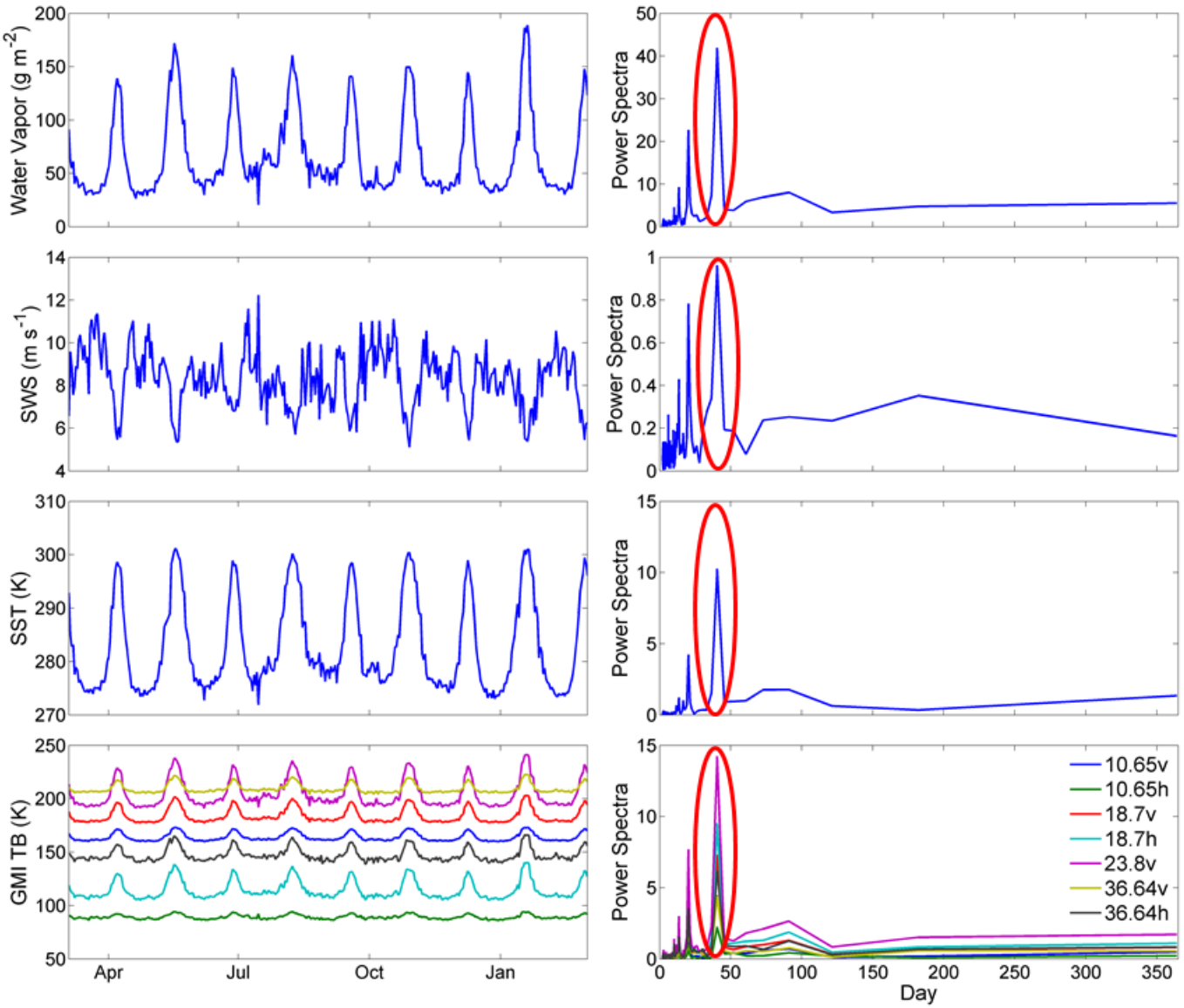

Figure 4. Time series of geophysical parameters (water vapor, SWS, and SST) and TB. The 40 day signal is also found.

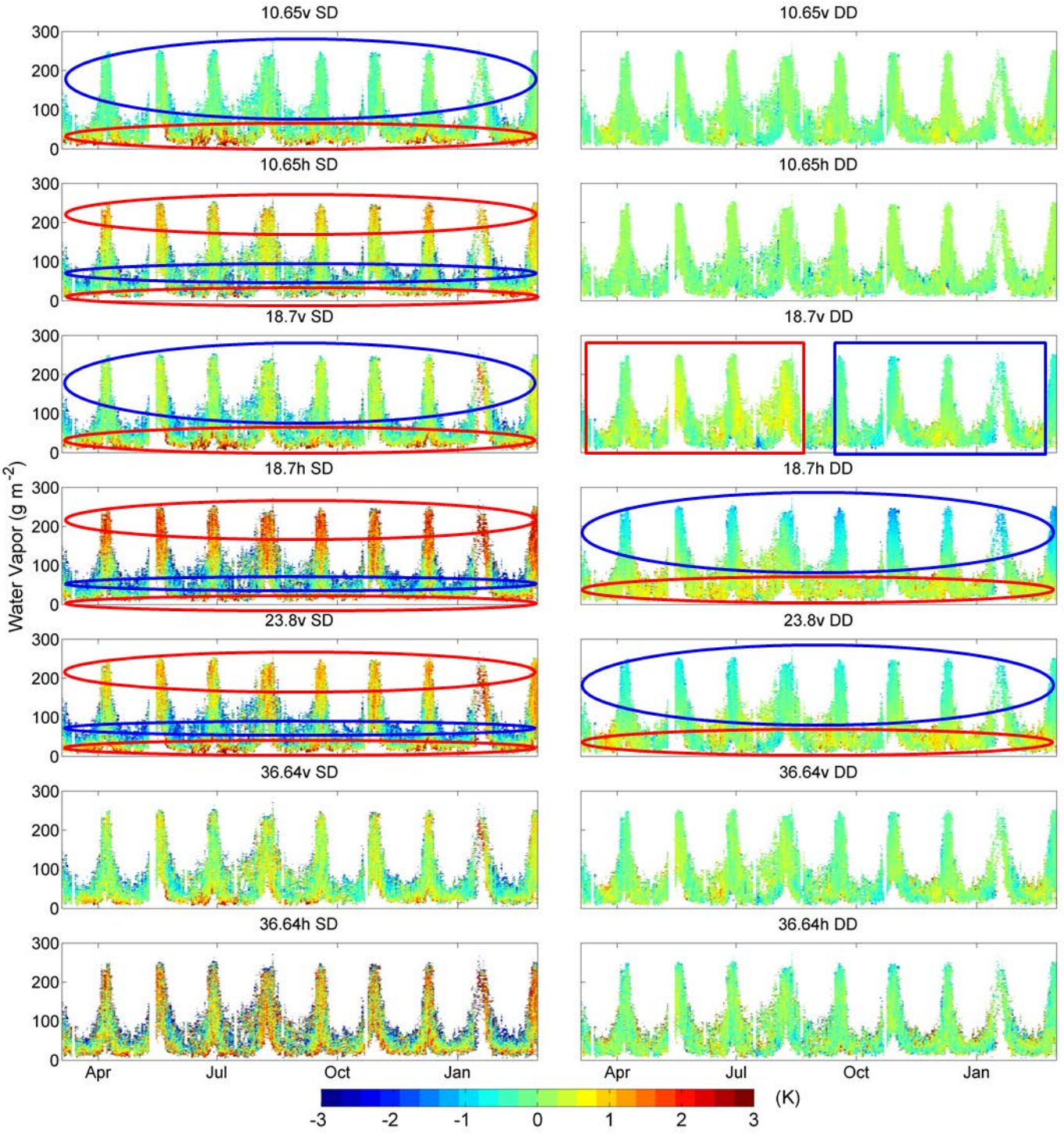

Figure 5. The temporal variability of water vapor dependent single (GMI) and double difference (GMI/WindSat). The positive and negative departures are highlighted, showing different types of dependence with different channels. Single difference shows monotonic negative dependence on water vapor in channel 10.65Vand 18.7V, non-monotonic dependence in 10.65H, 18.7H and 23.8V, and relatively neutral in 36.64V&H. Double difference can have opposite monotonicity as single difference.

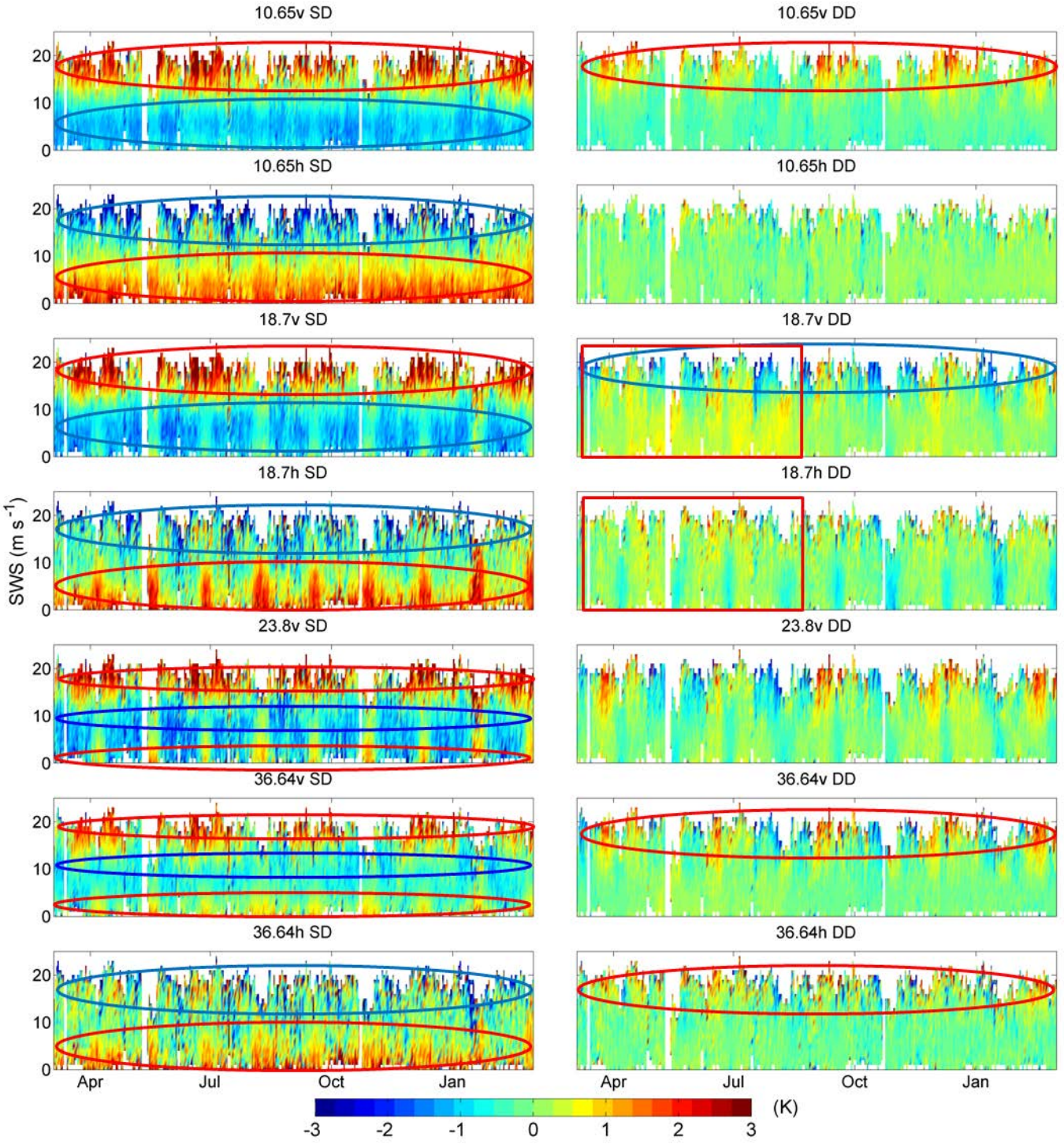

Figure 6. The temporal variability of SWS dependent single (GMI) and double difference (GMI/WindSat) with highlighted positive or negative departures. SWS also has a significant impact on calibration with monotonic or non-monotonic features.

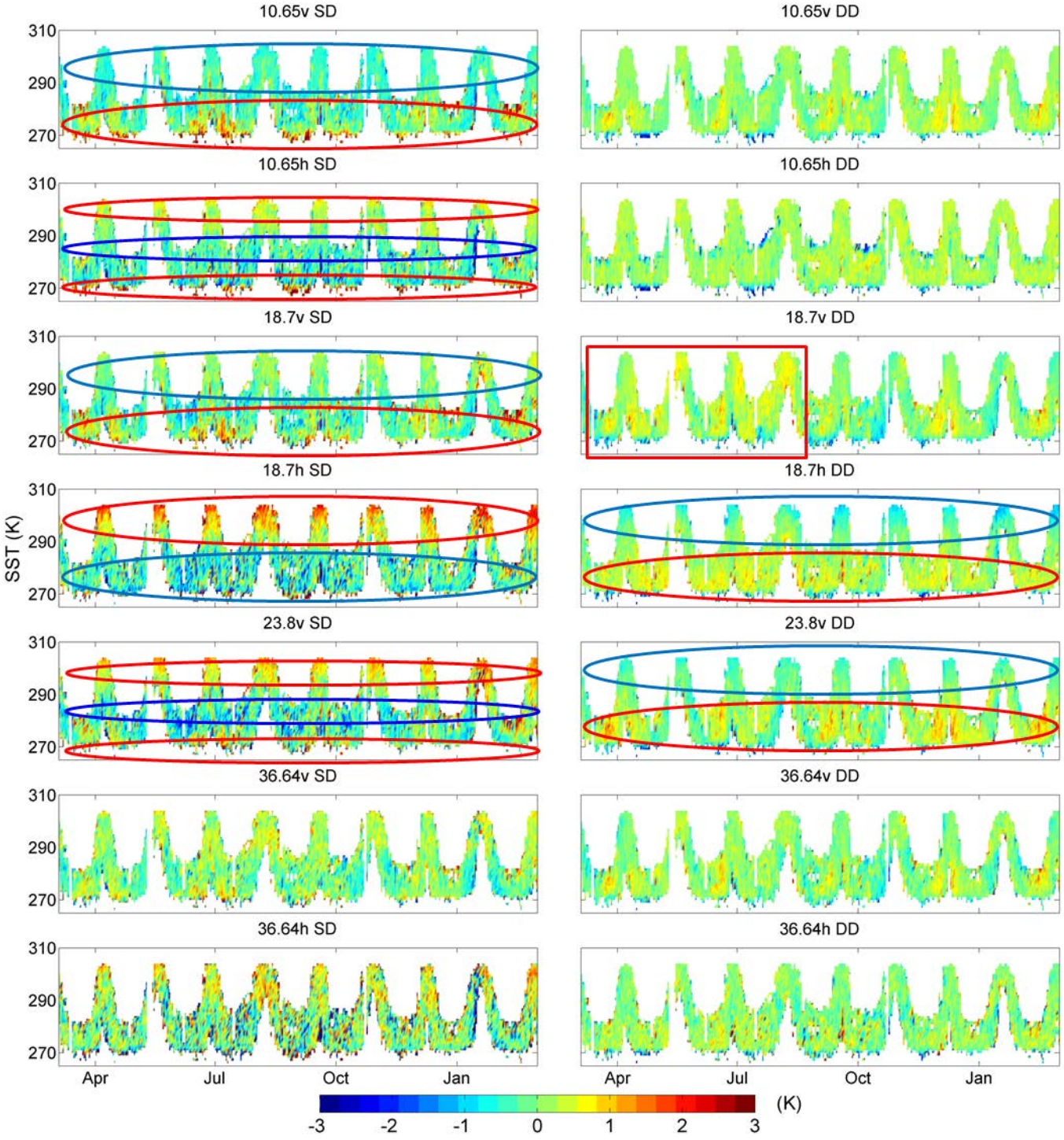

Figure 7. The temporal variability of SST dependent single (GMI) and double difference (GMI/WindSat) with highlighted positive or negative departures.

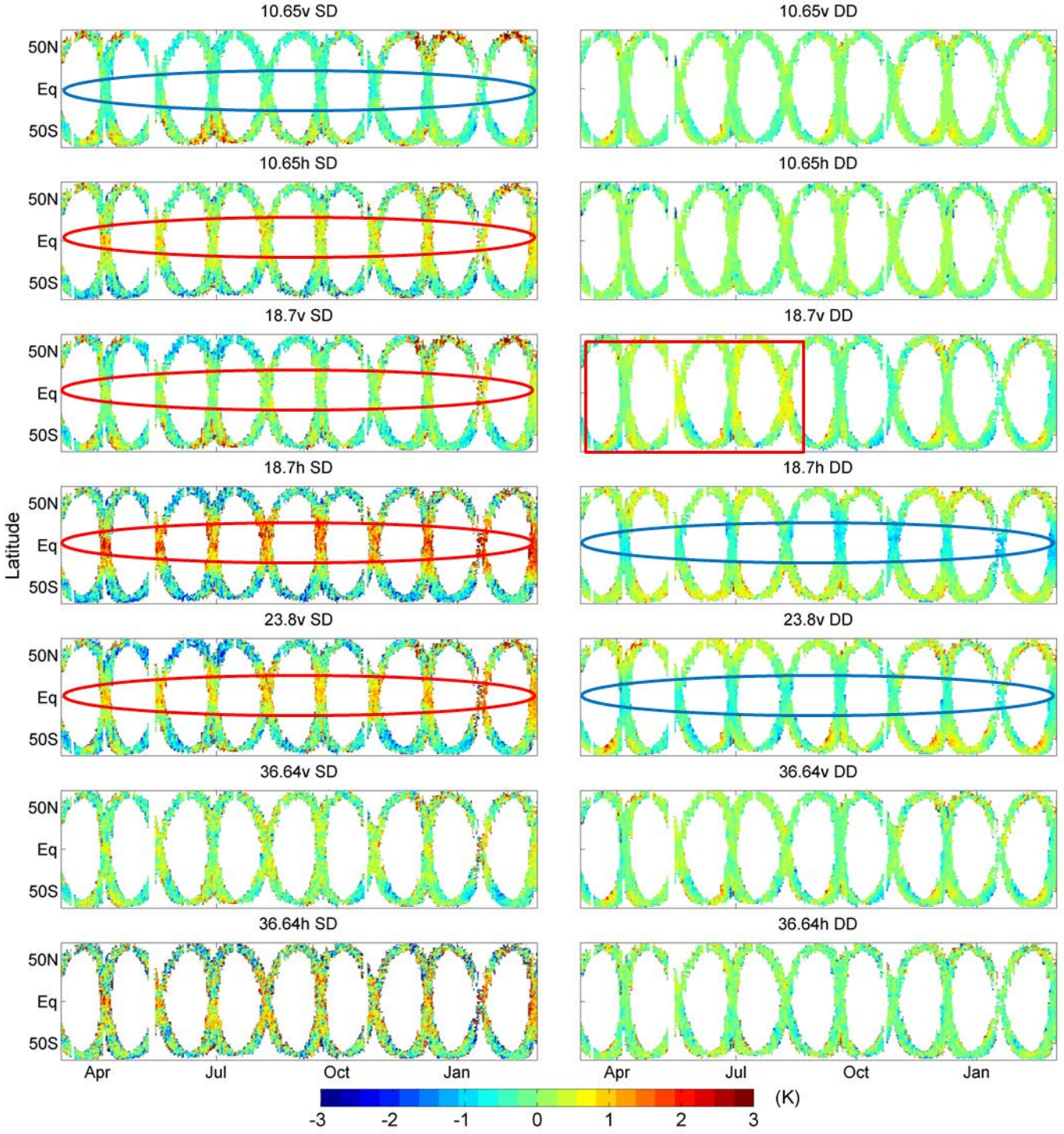

Figure 8. The temporal variability of latitude dependent single (GMI) and double difference (GMI/WindSat) with highlighted positive or negative departures. The latitudinal dependence is significant. It is consistent with temporal variability and can be opposite between single and double differences.

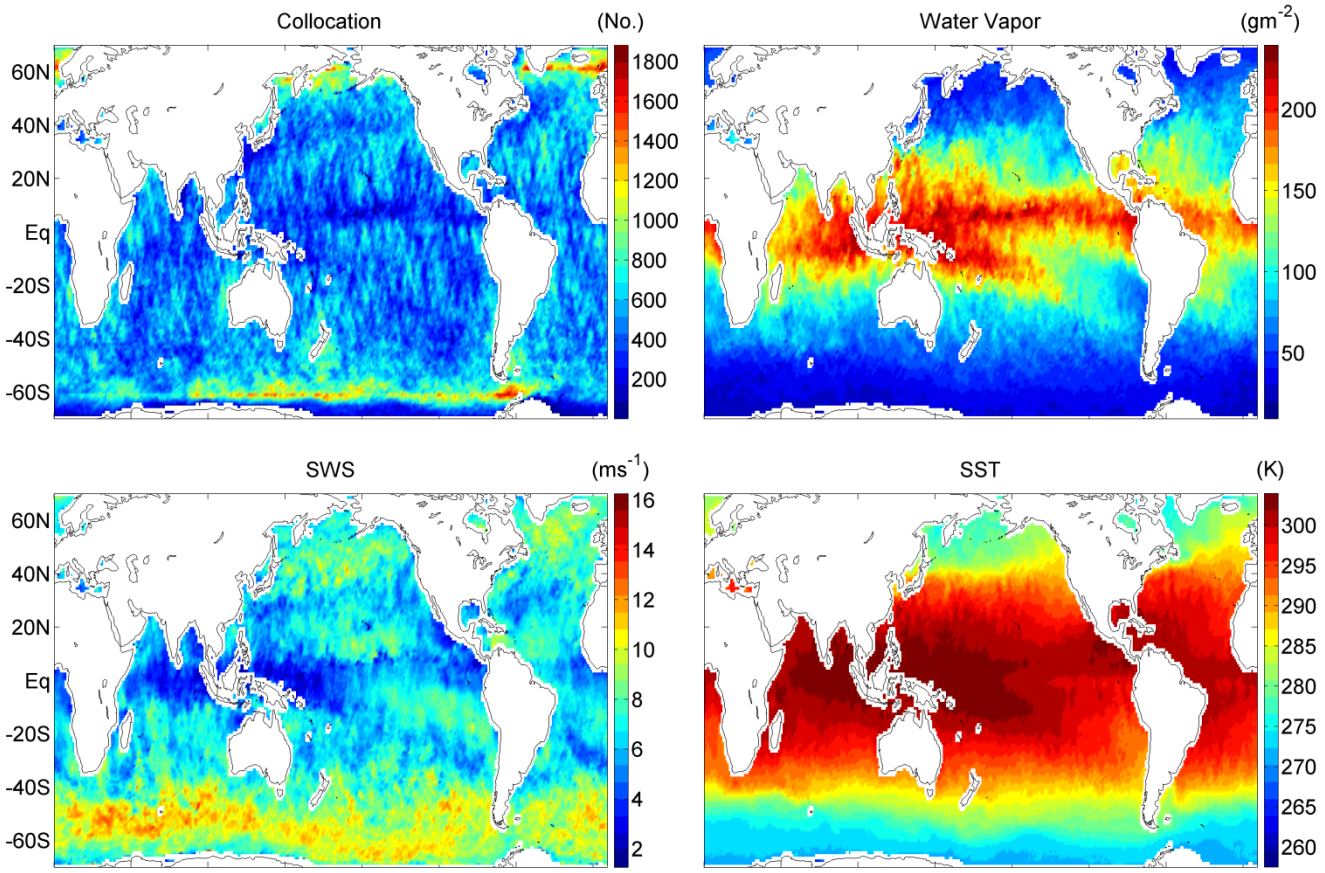

Figure 9. The maps of collocation number, water vapor, SWS and SST. The geophysical parameters have pronounced regional dependence and affect calibration.

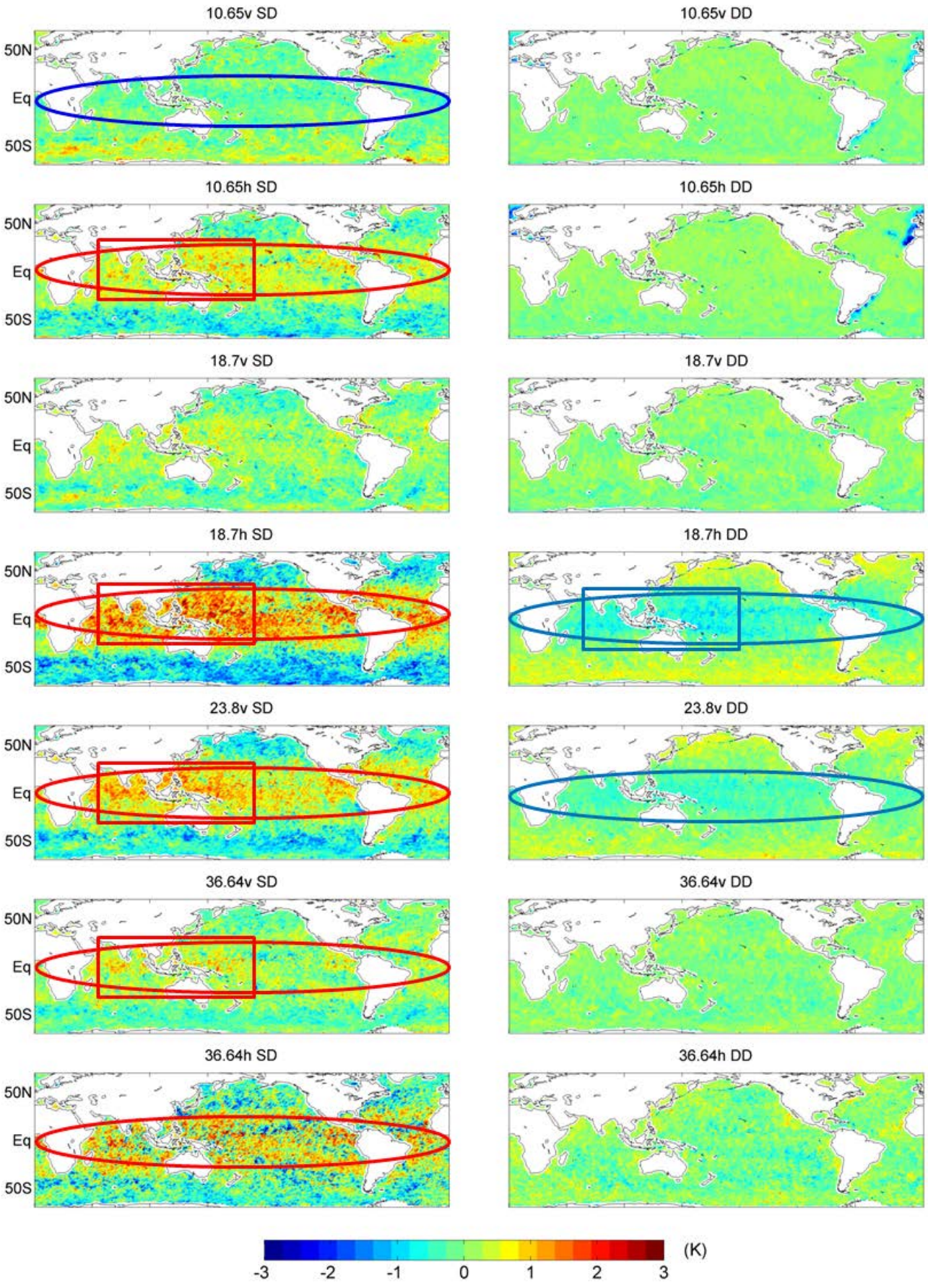

Figure 10. The maps of single (GMI) and double difference (GMI/WindSat). The positive and negative departures are highlighted and show latitudinal and longitudinal dependence. The spatial variability resembles that of geophysical parameters particularly water vapor and SWS. The noticeable negative departure of double difference at 10V and 10H is seen near coastal regions such as Europe, West America and East America, which is due to the large FOVs of WindSat that result in land contamination and large WindSat single difference.

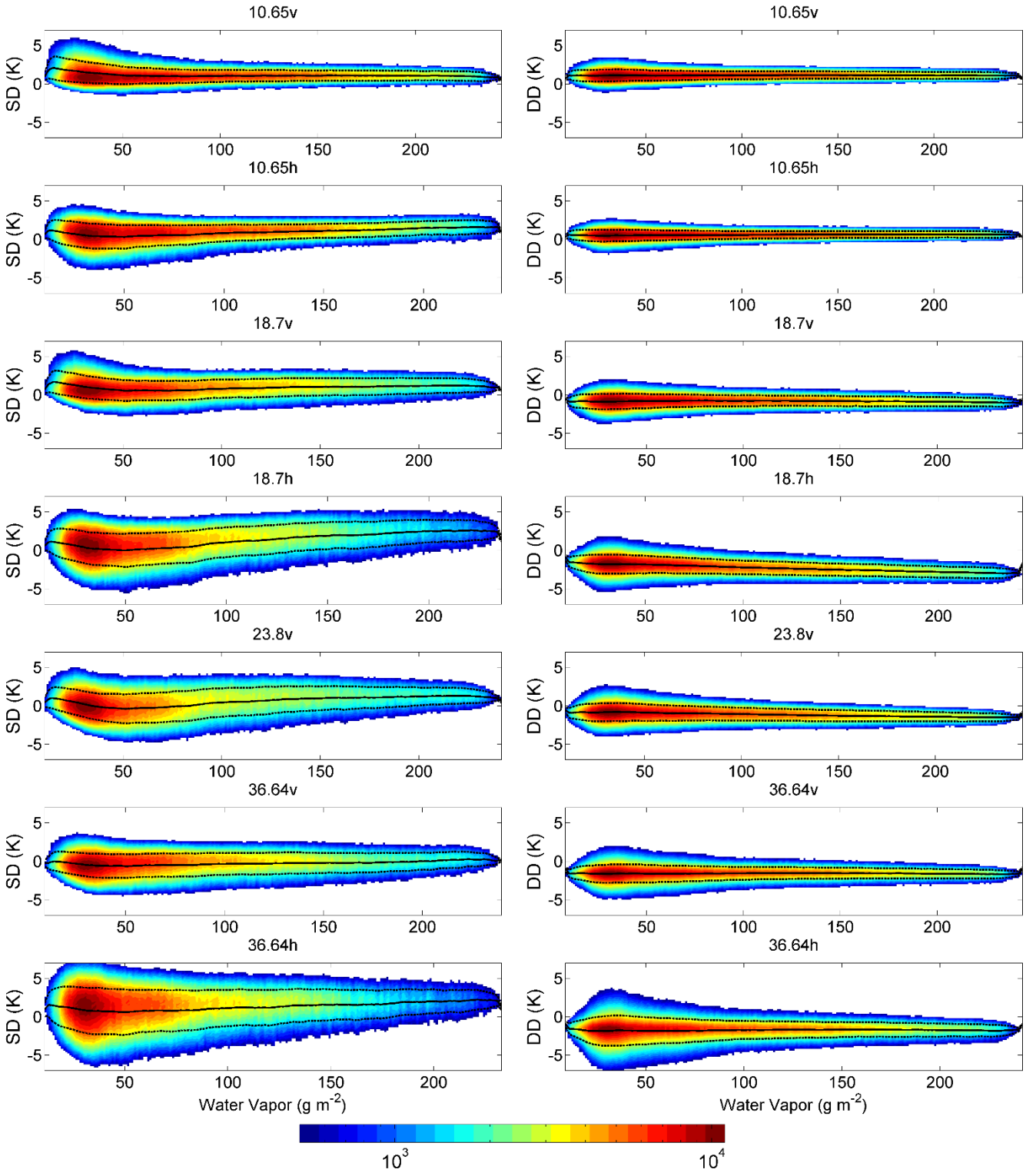

Figure 11. The dependence of single (GMI) and double difference (GMI/WindSat) on water vapor. The solid and dash lines show mean and standard deviation (plus and minus) with maximum standard deviations 3.1 and 2.0 K at 36.6H. Nonlinear and non-monotonic dependence is found with bump in the middle and drops at both ends.

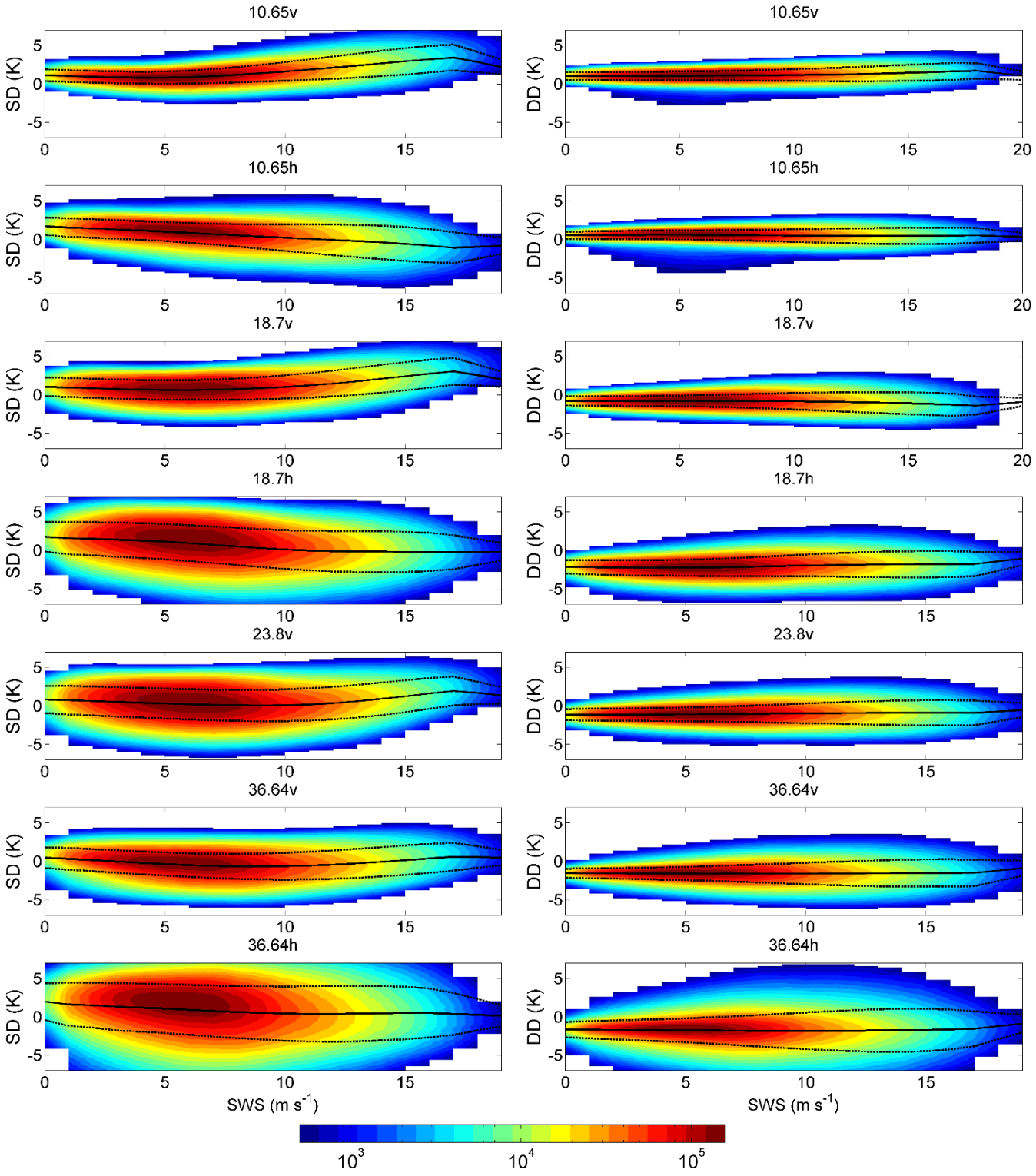

Figure 12. The dependence of single (GMI) and double difference (GMI/WindSat) on SWS. Nonlinear and non-monotonic dependence is noticeable. The single differences in V-pol and H-pol channels show overall opposite trends that are positive and negative respectively. The uncertainties are larger than that of water vapor with maximum standard deviations of 3.7 and 2.9 K for single and double differences respectively.

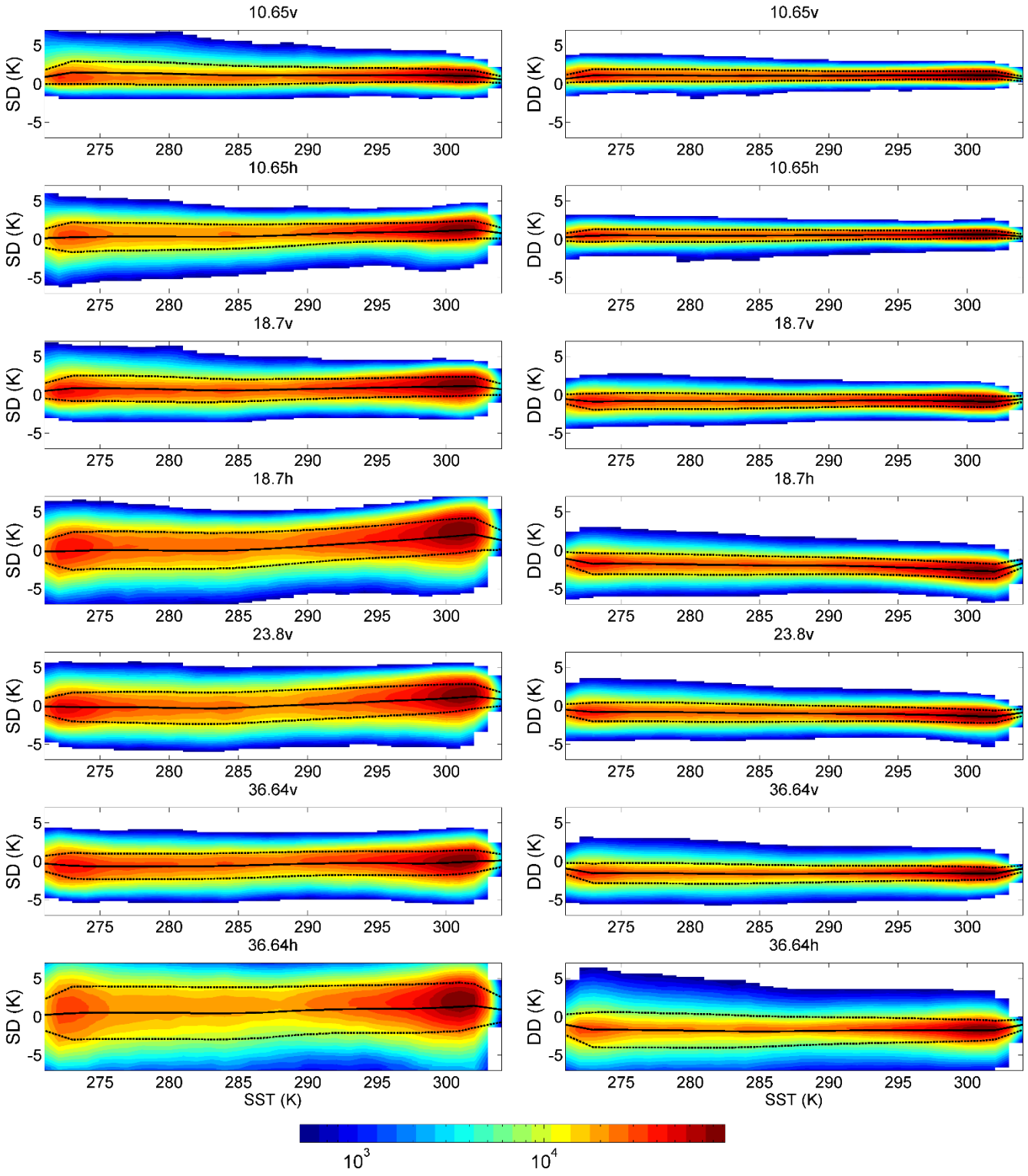

Figure 13. The same as Figure 12 but for SST. SST has two modes with a number of samples at cold (270-277ºC) and warm (300-305ºC) SSTs. The nonlinearity and non-monotonicity are noticeable but smaller than that of water vapor and SWS.

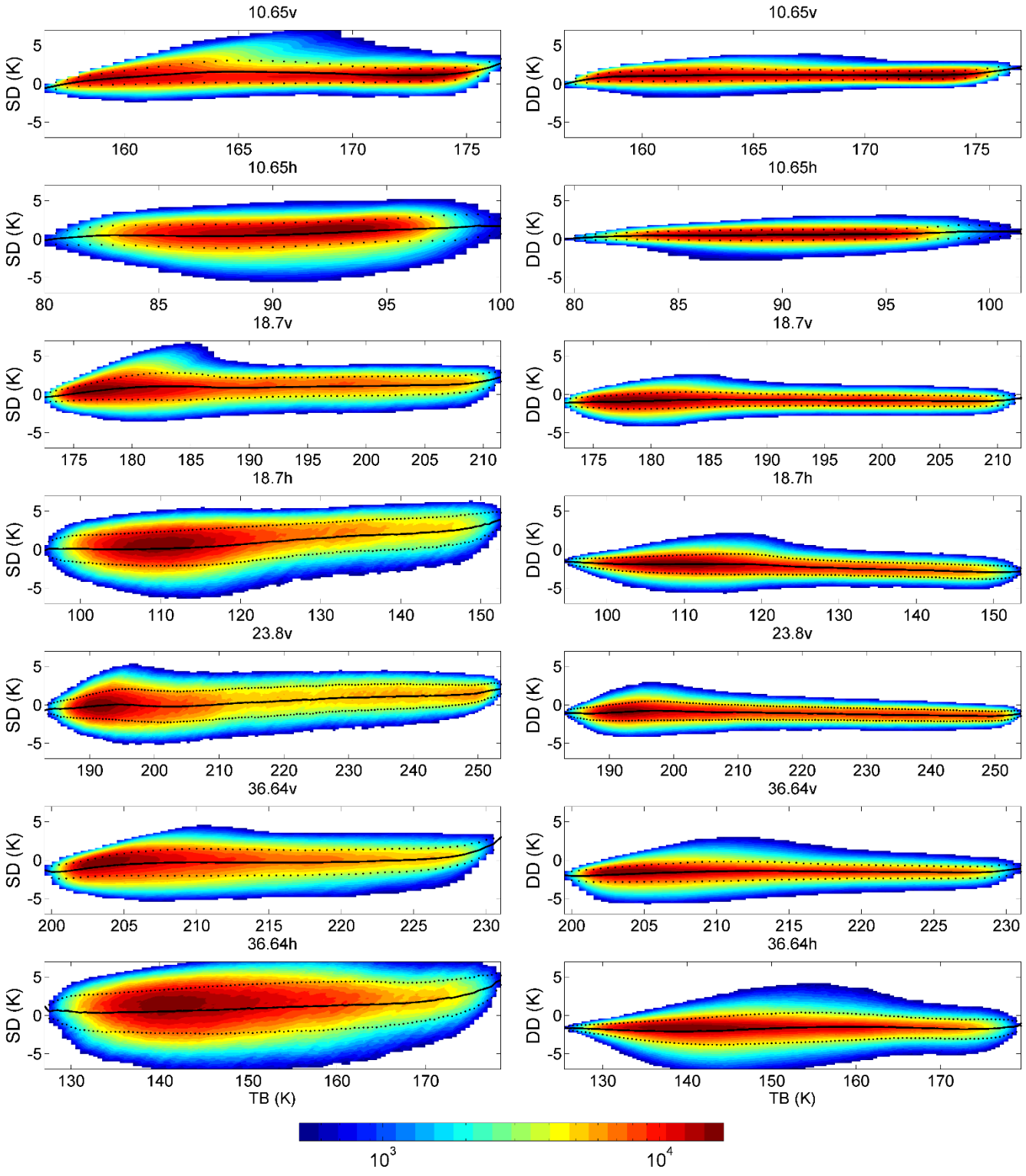

Figure 14. The single (GMI) and double difference (GMI/WindSat) as a function of TB. Since TB is a function of all geophysical parameters, the nonlinearity and non-monotonicity are more significant (maximum standard deviations are 3.1 and 2.0 K for single and double differences respectively) with mixing features from geophysical parameters.

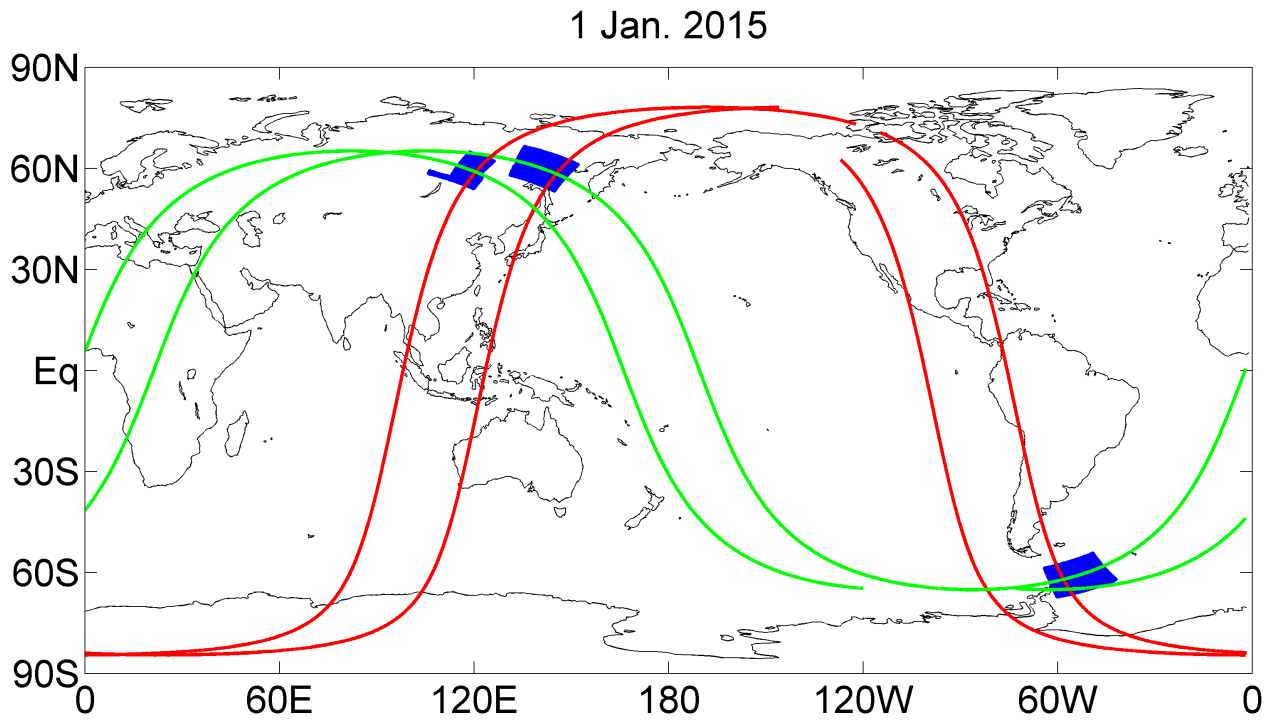

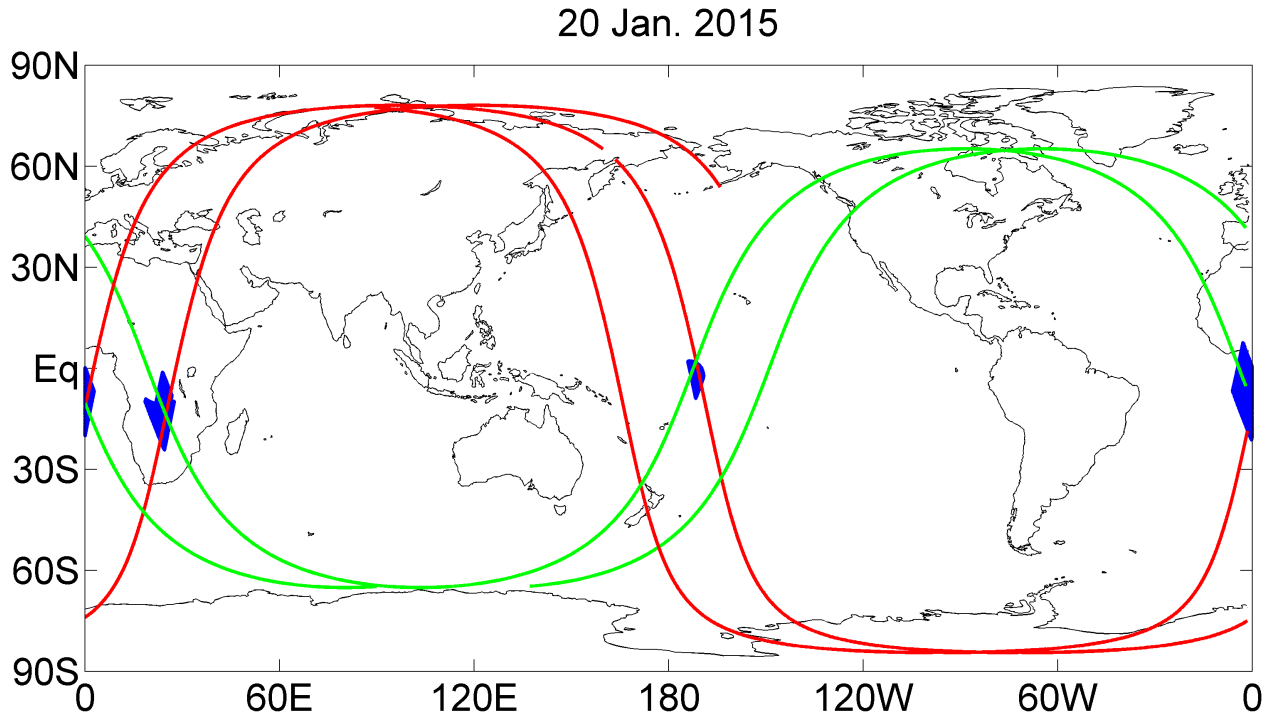

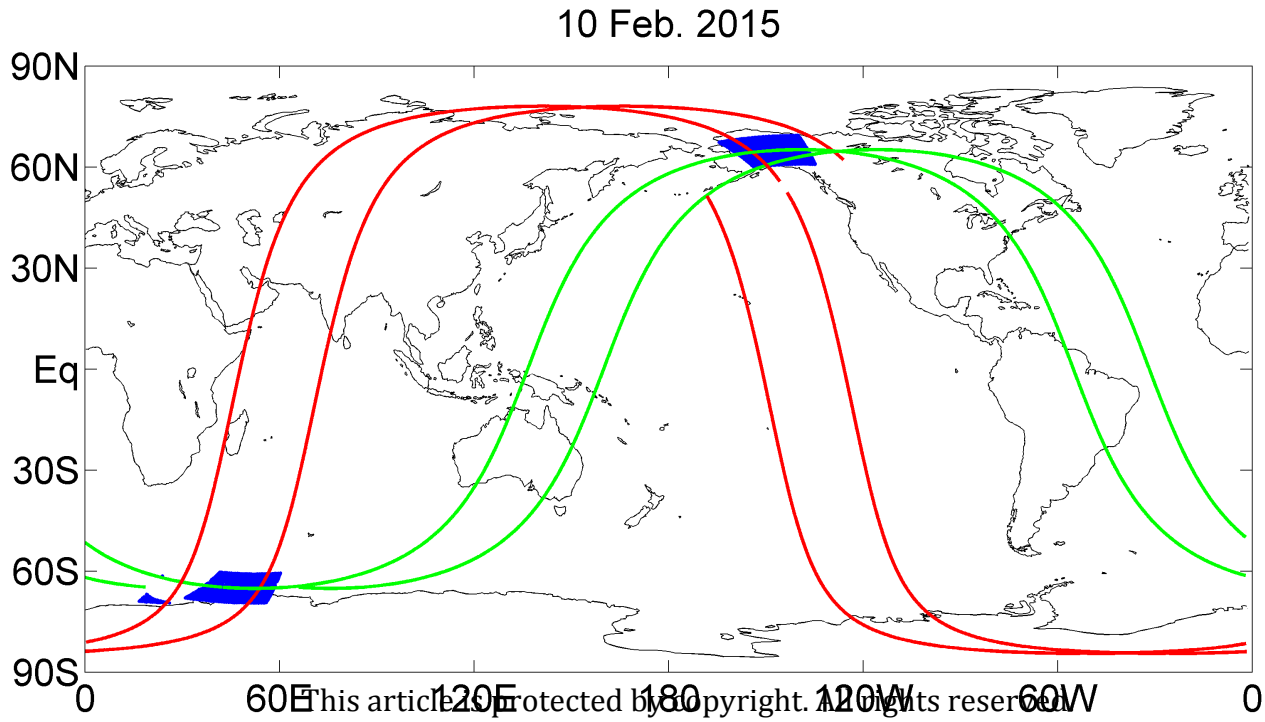

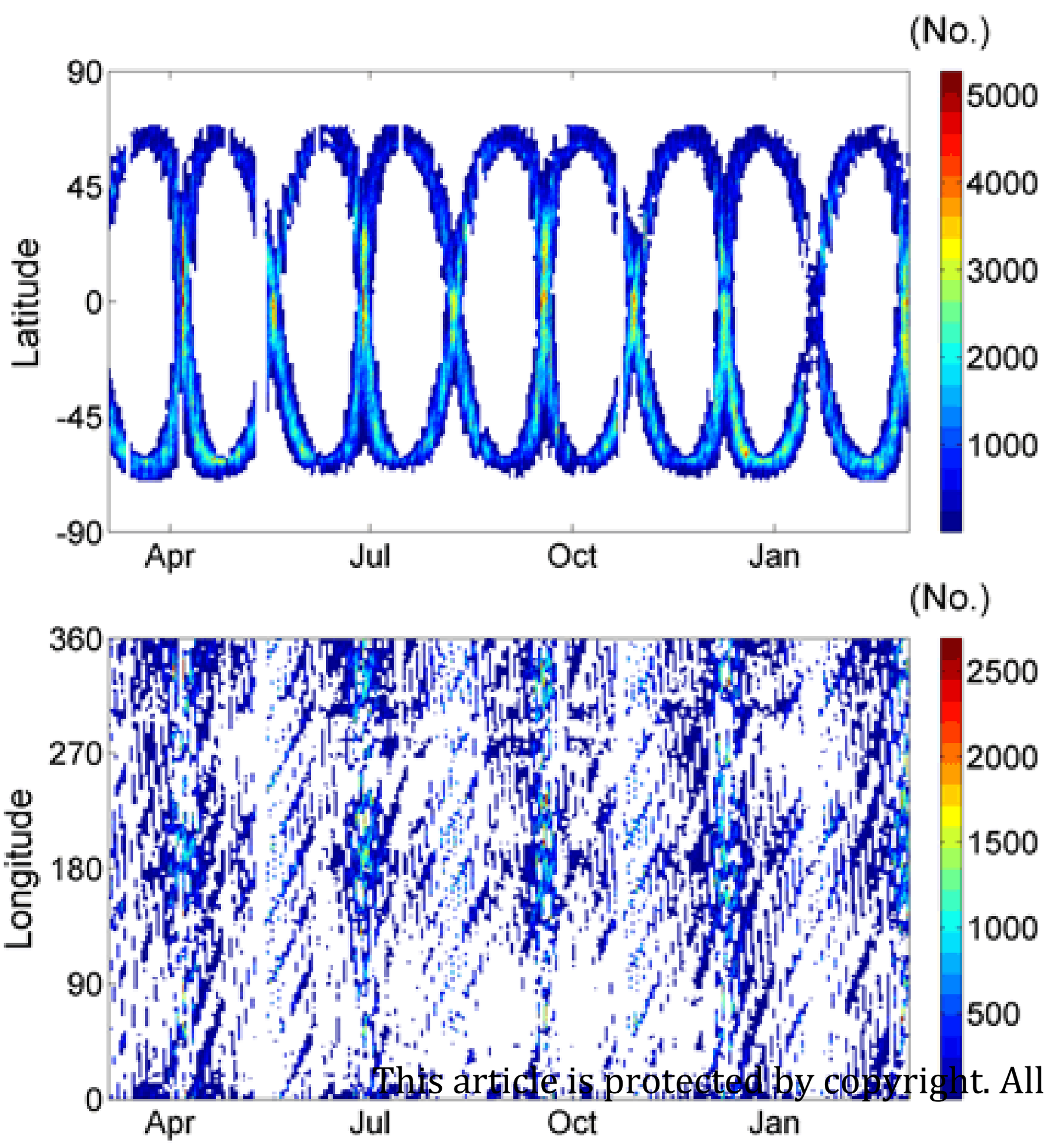

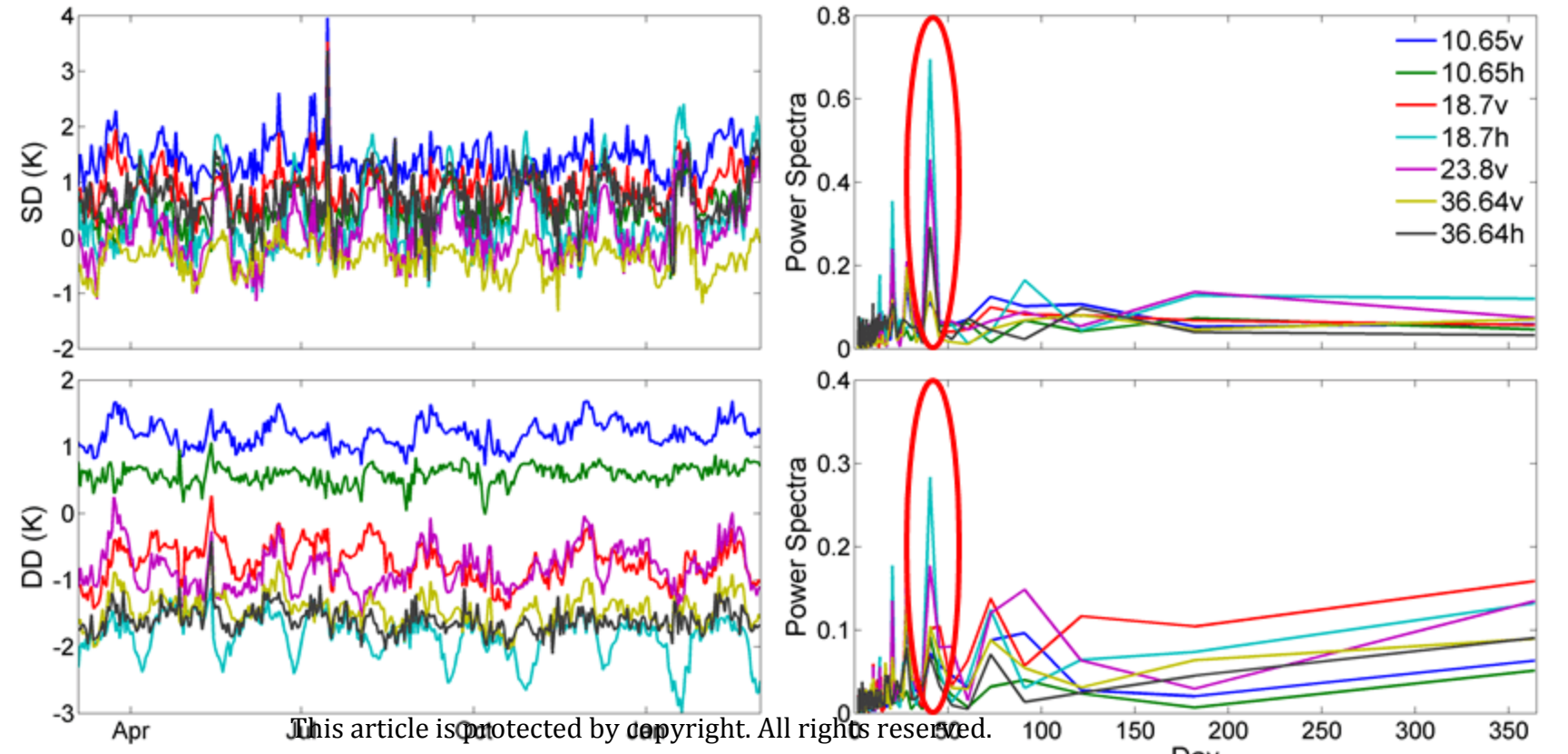

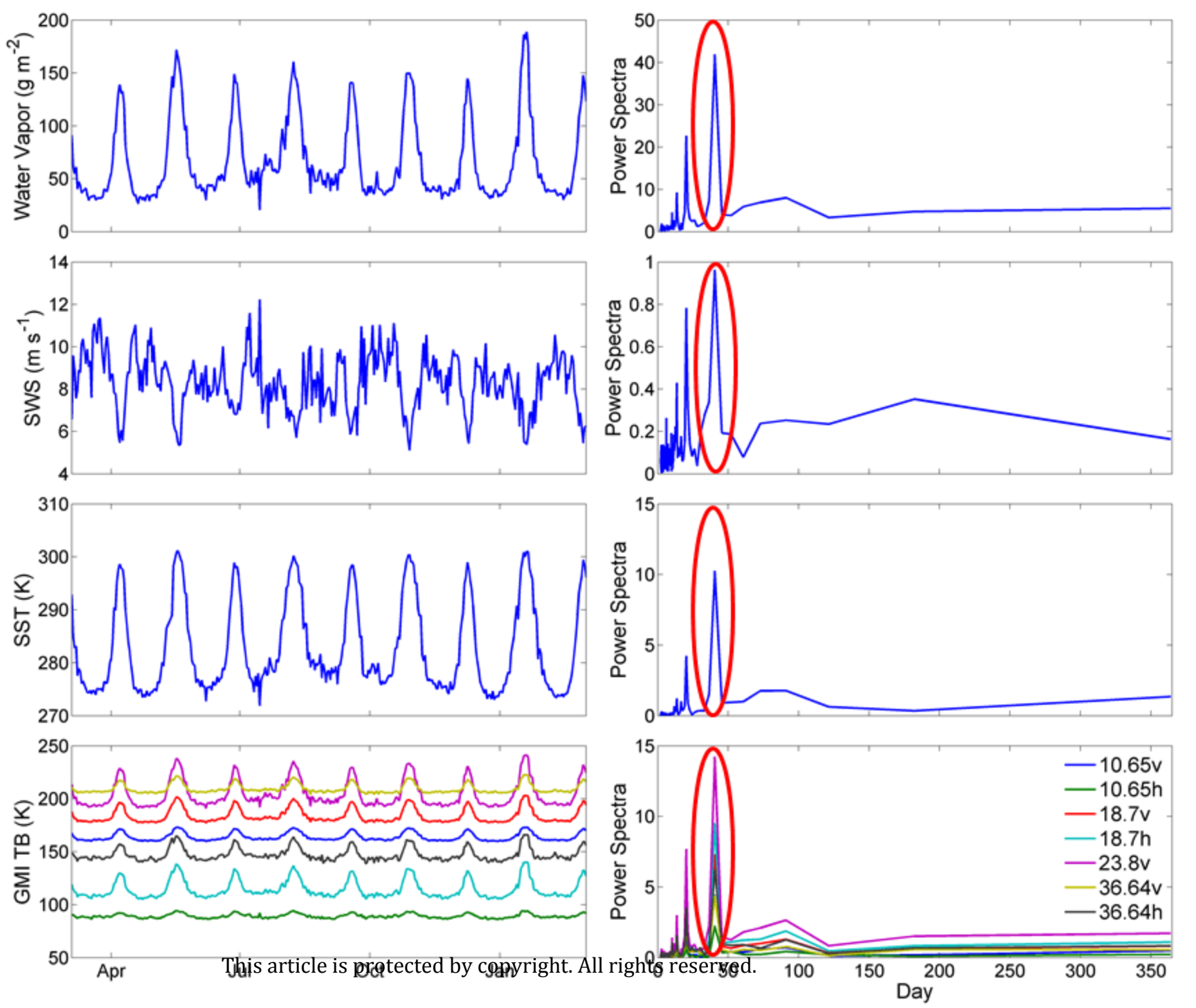

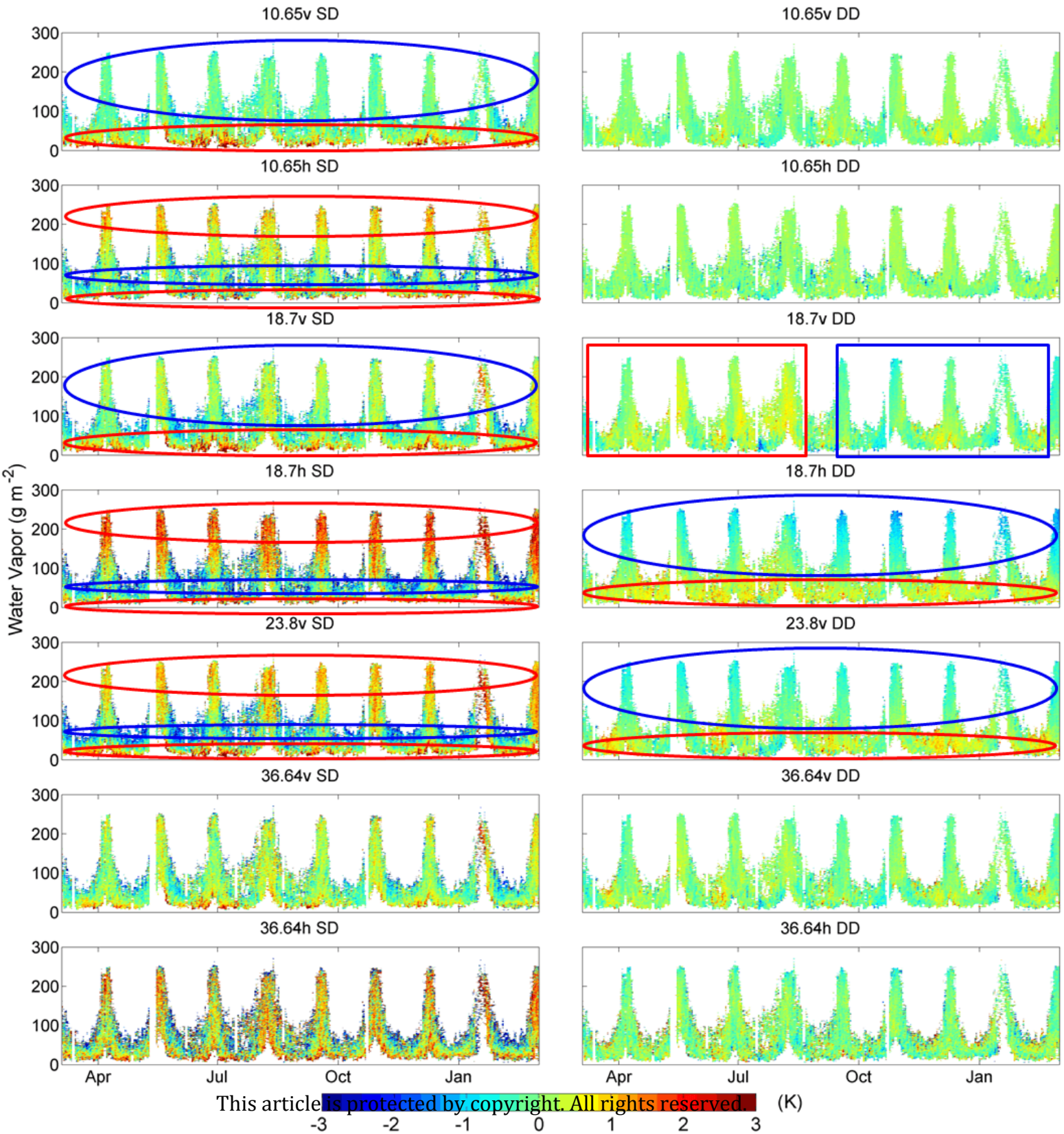

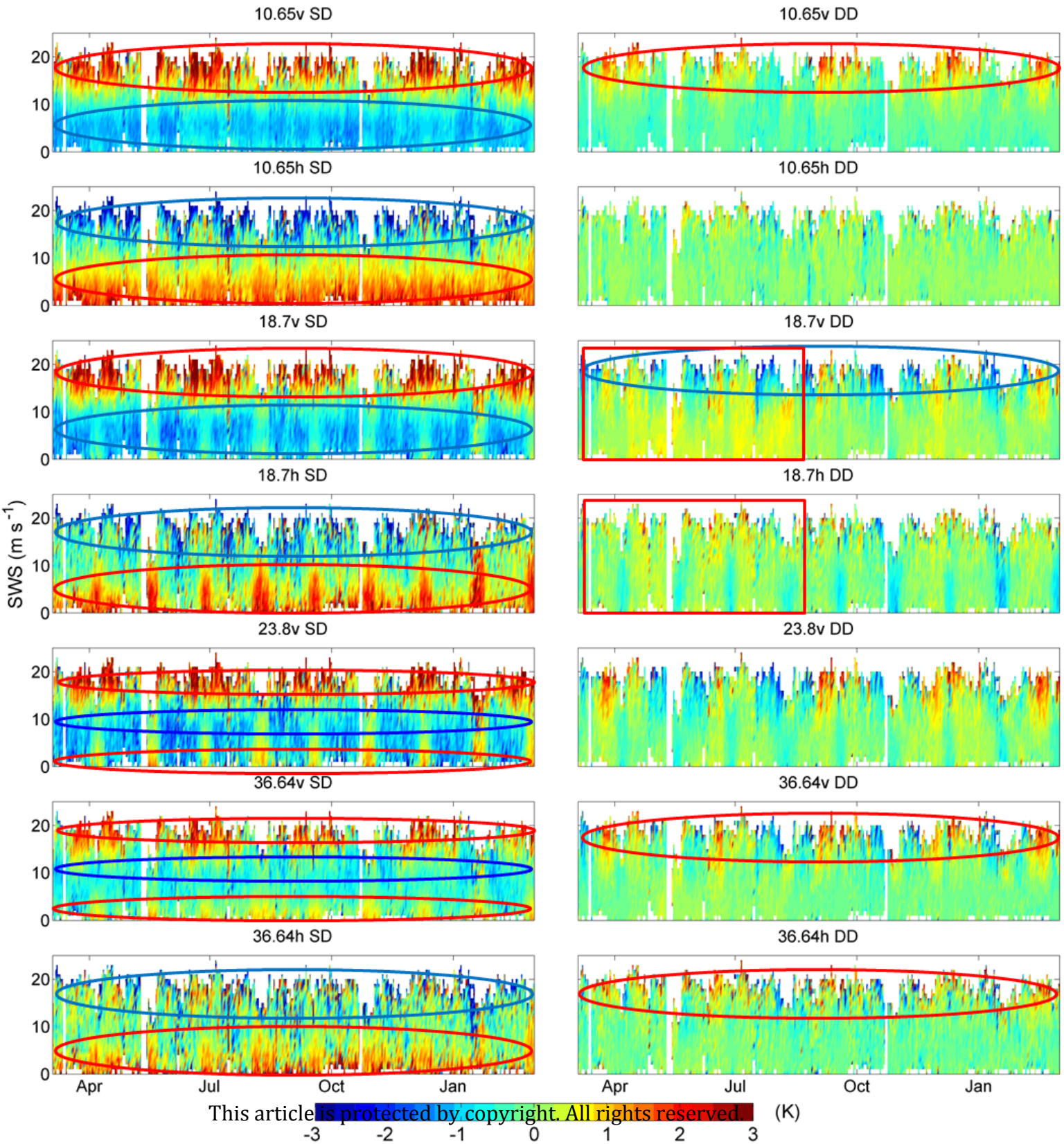

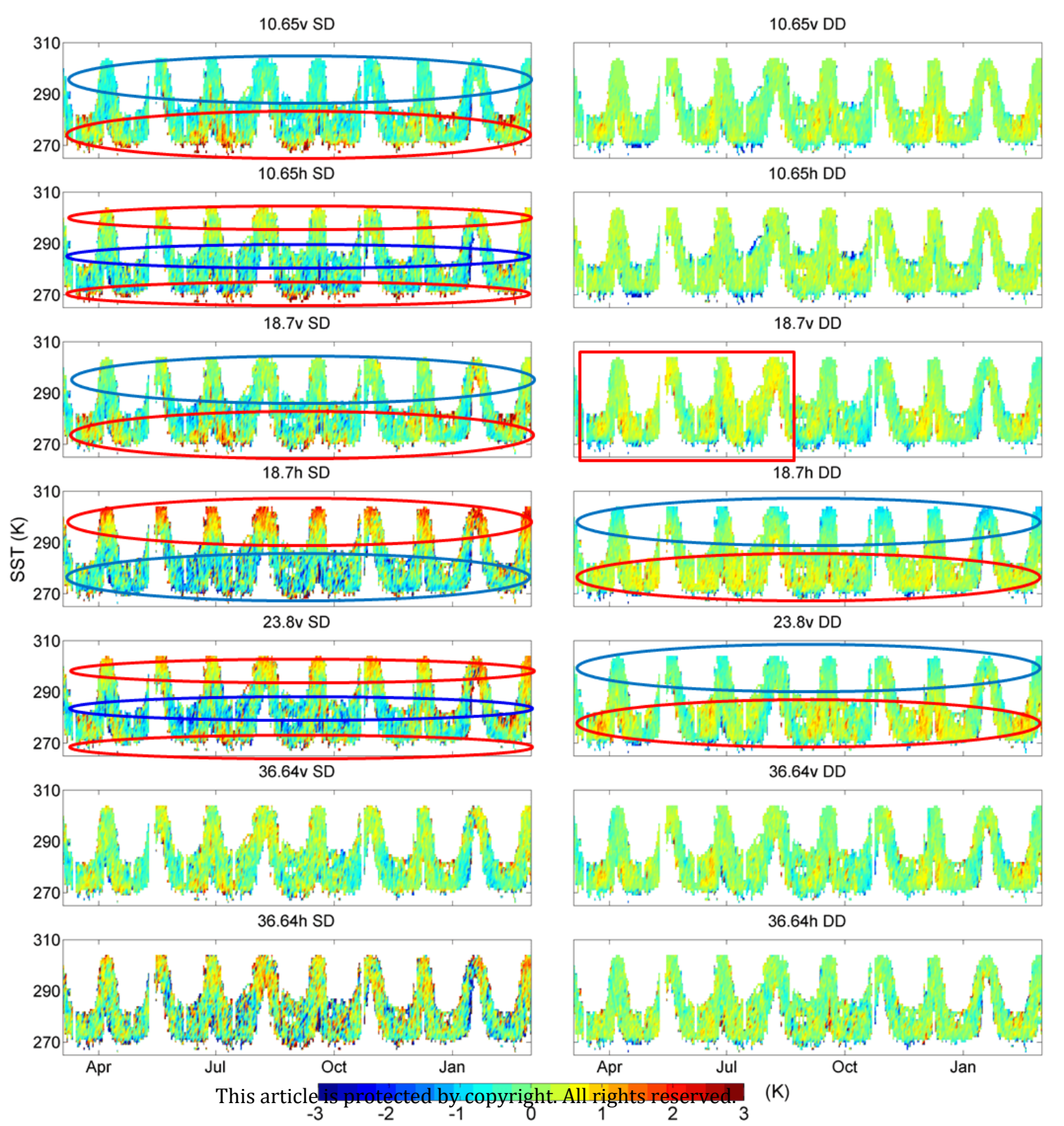

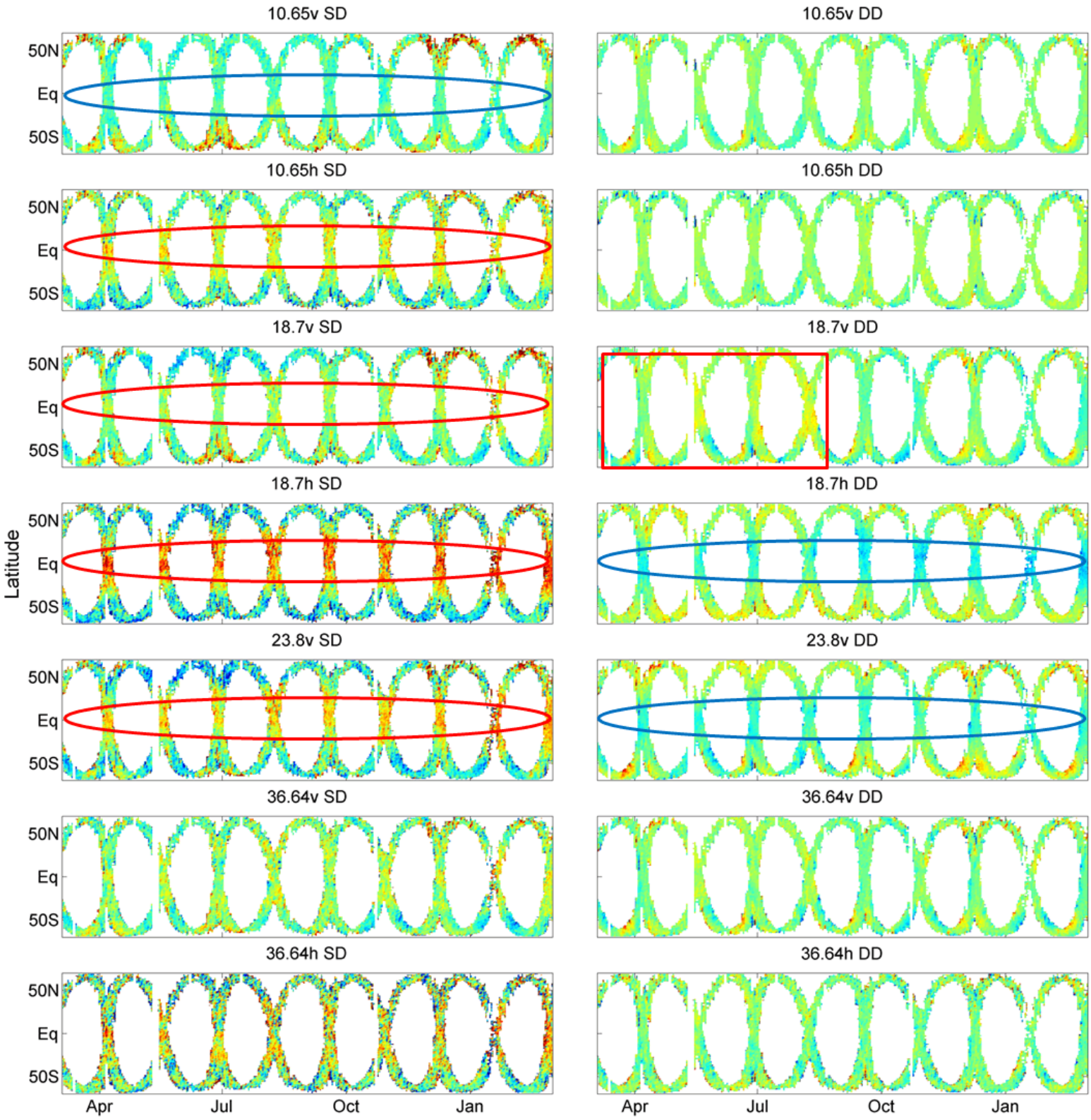

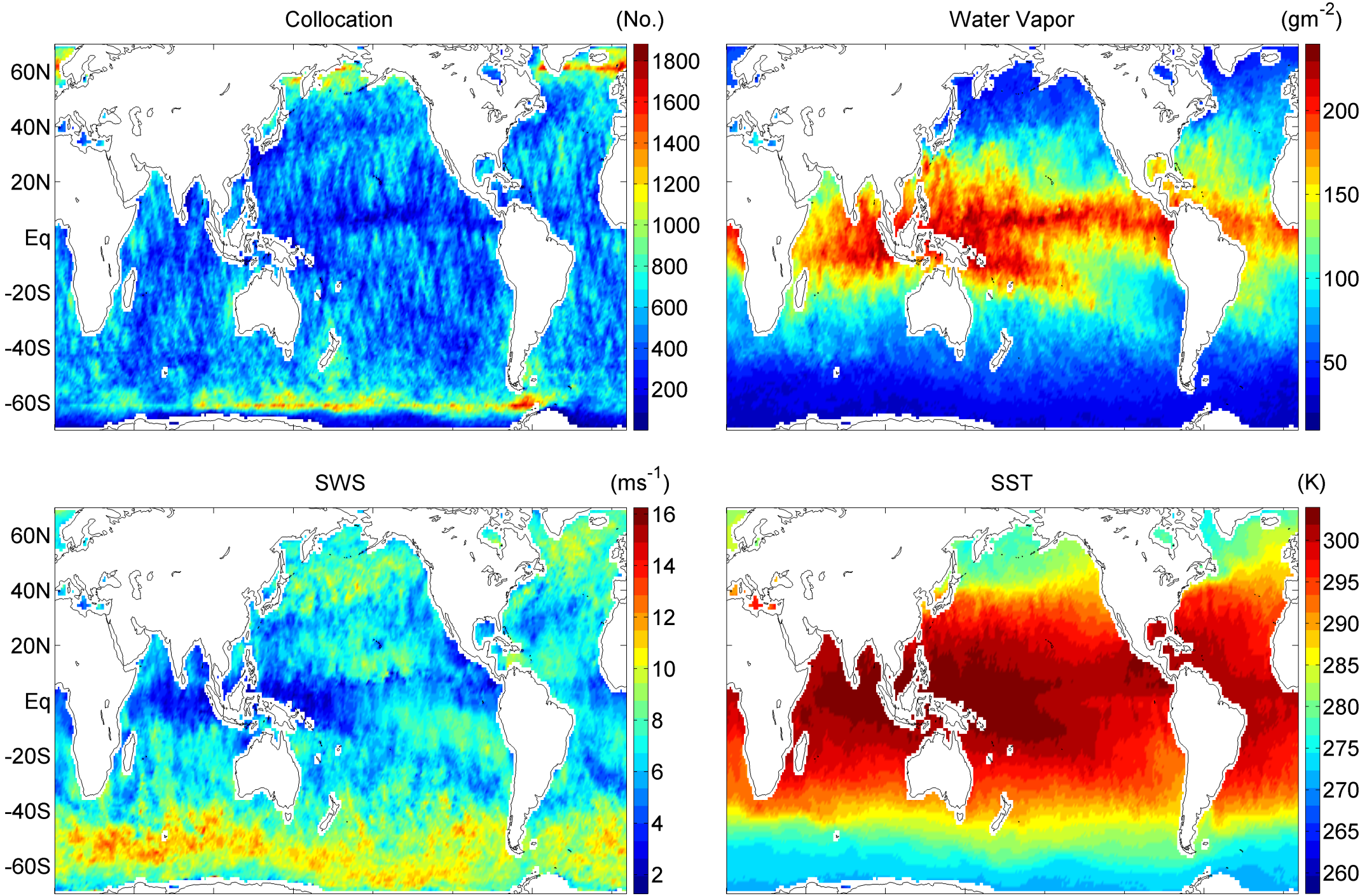

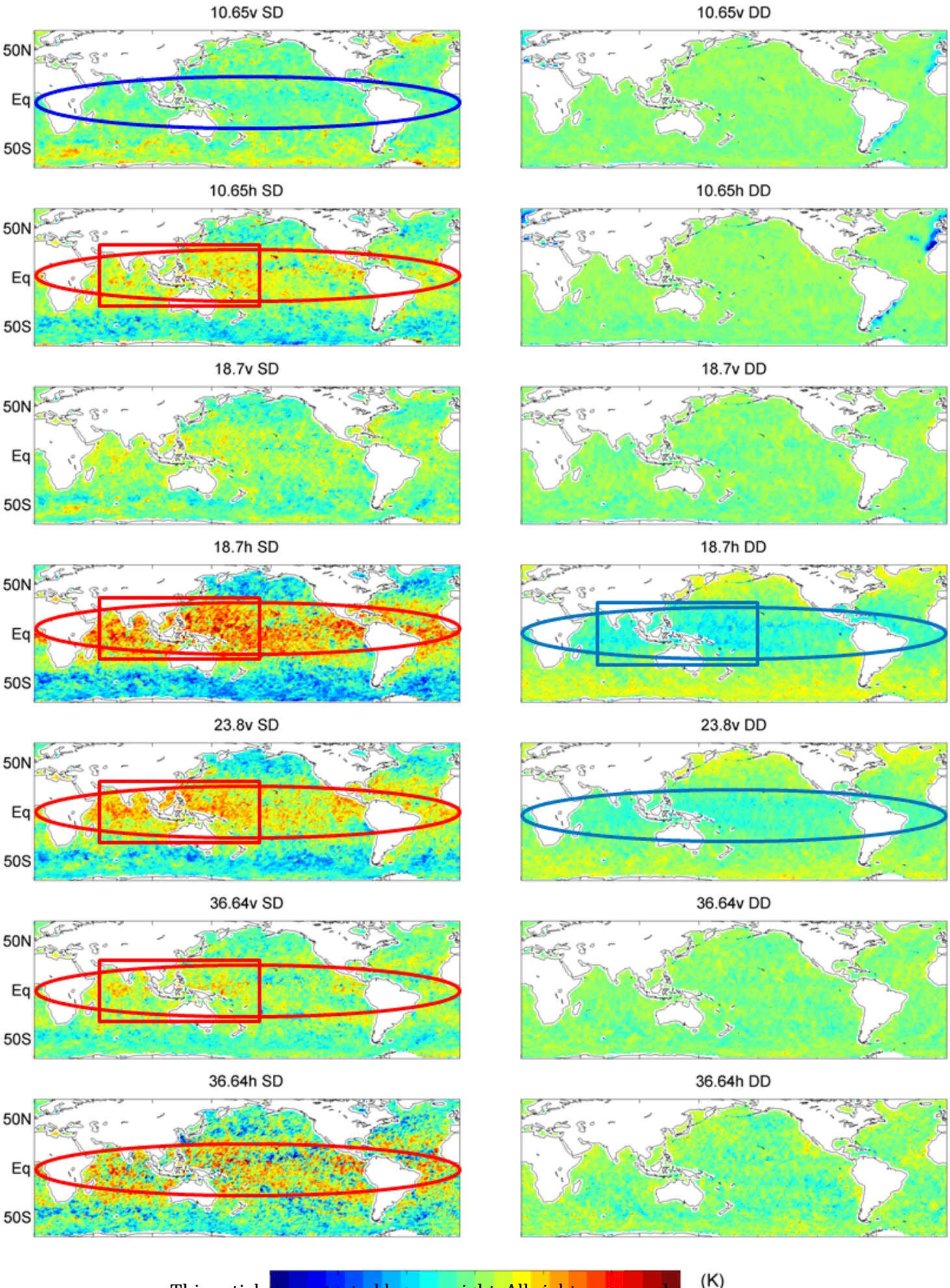

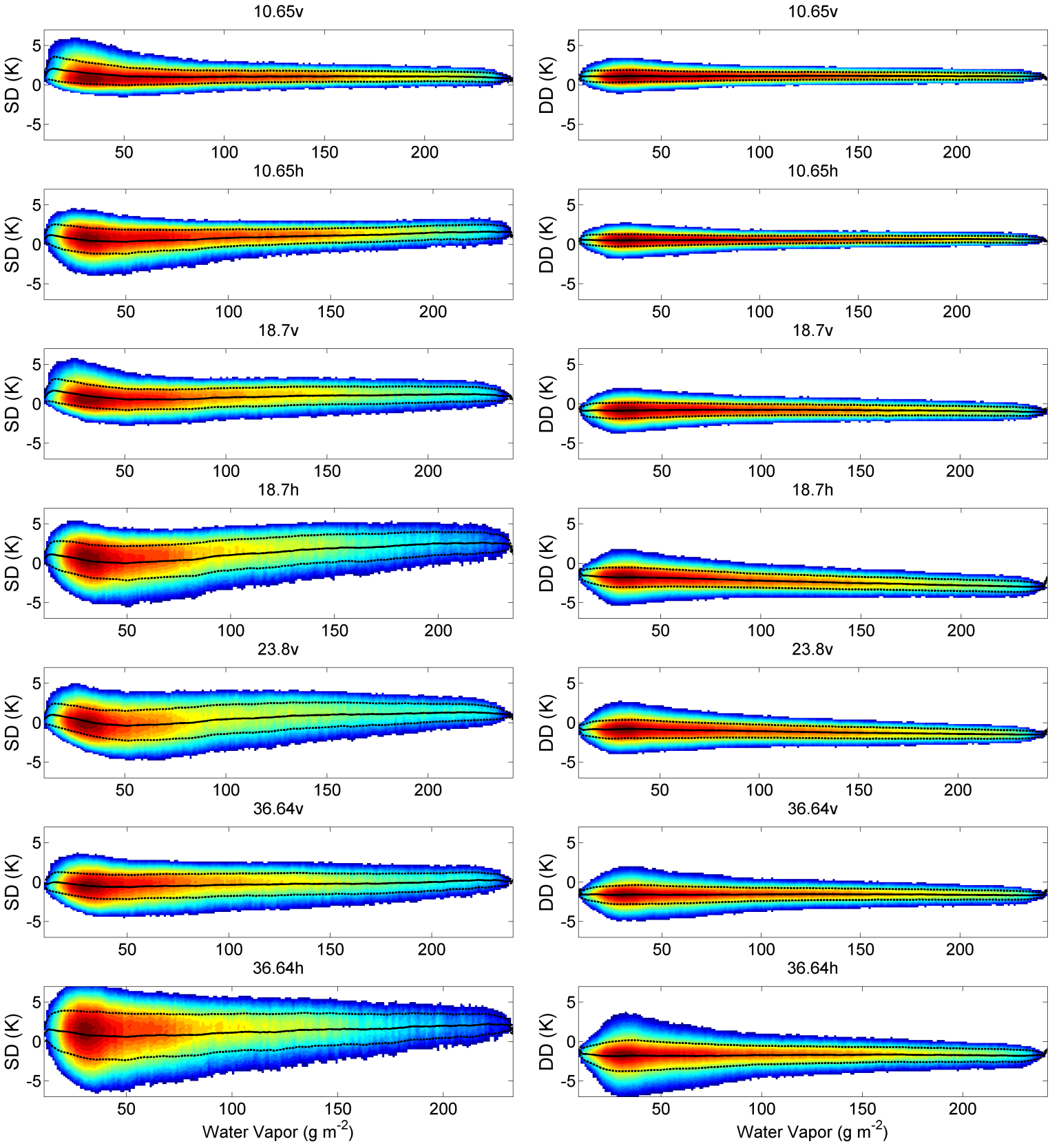

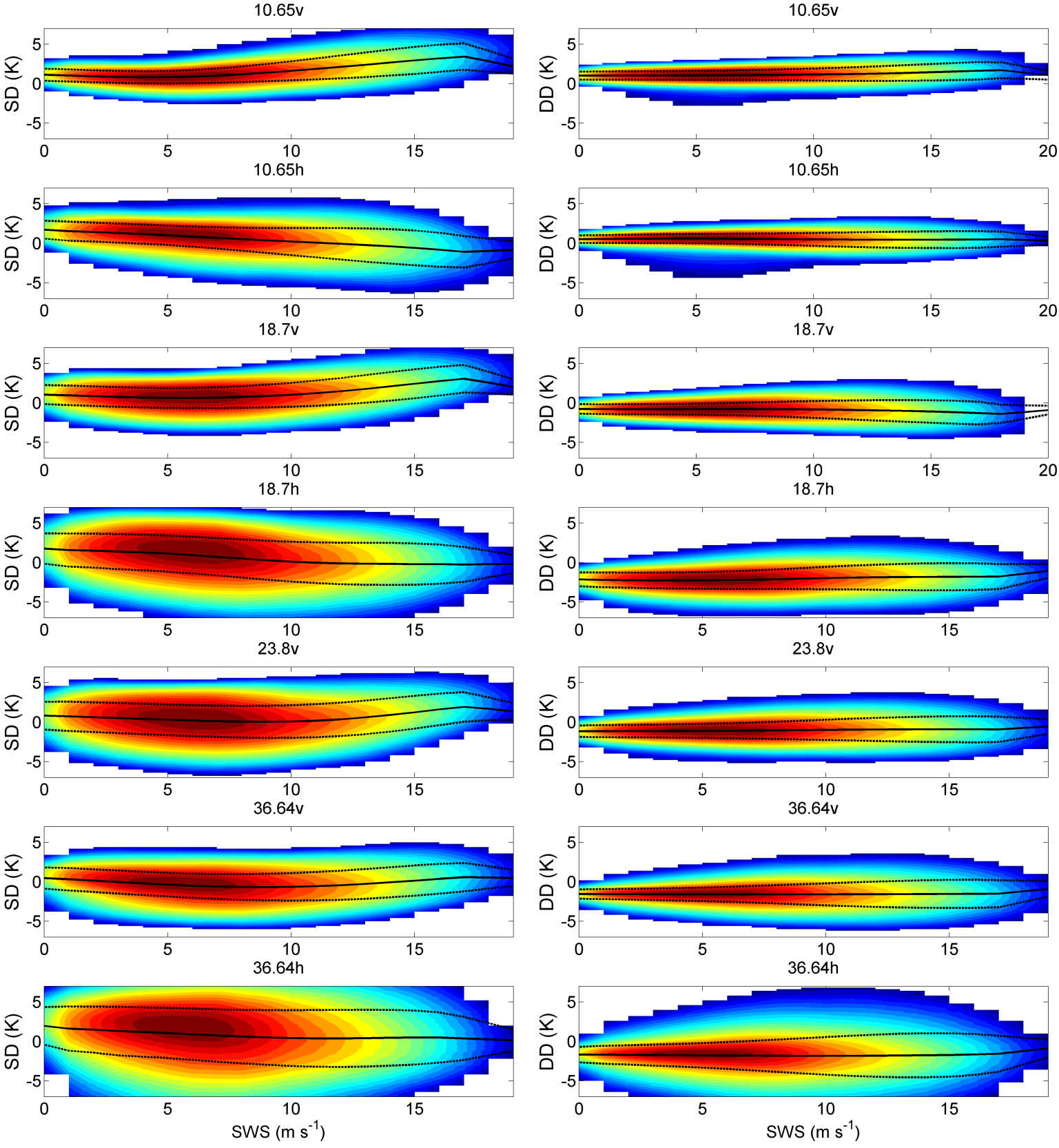

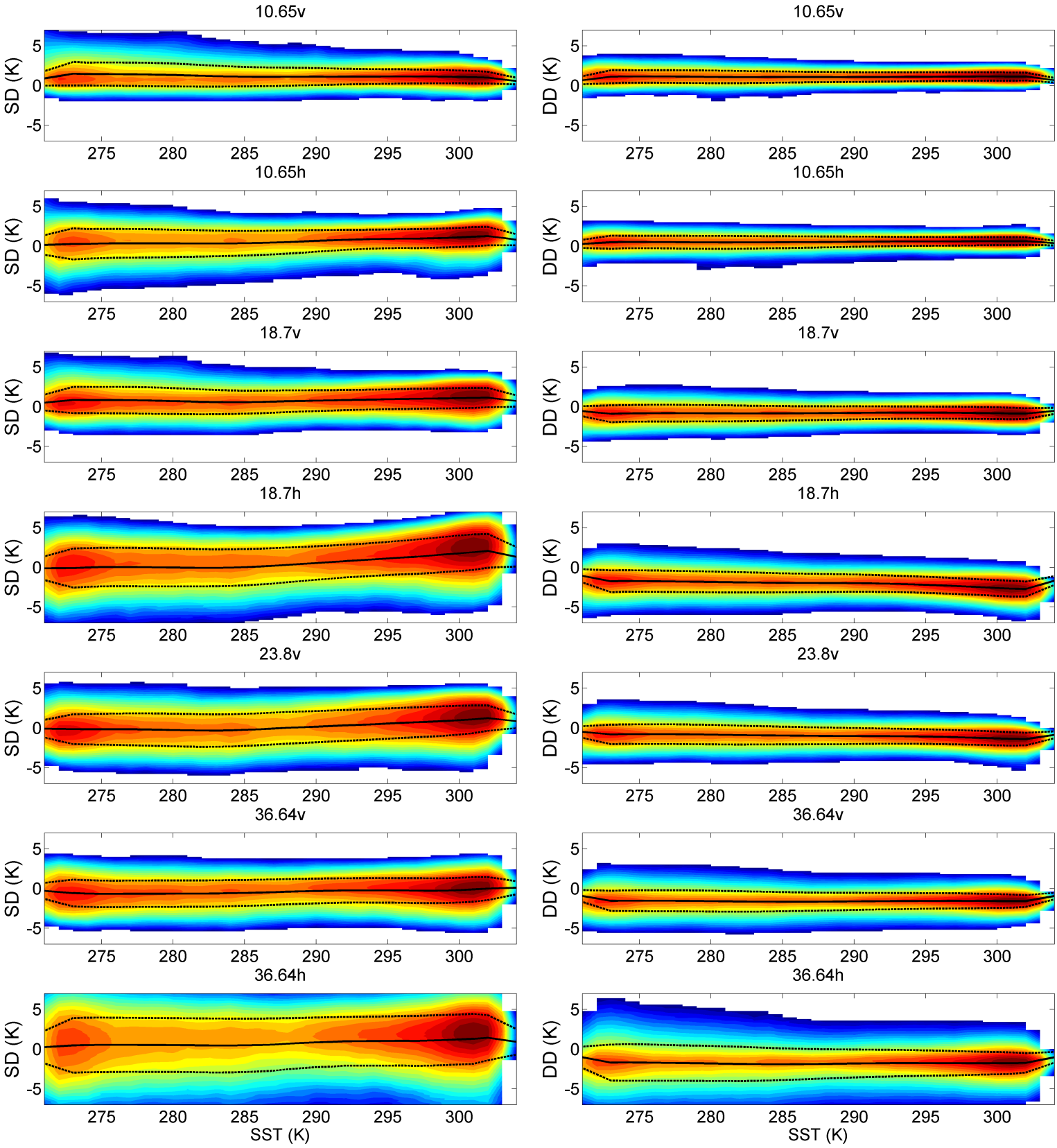

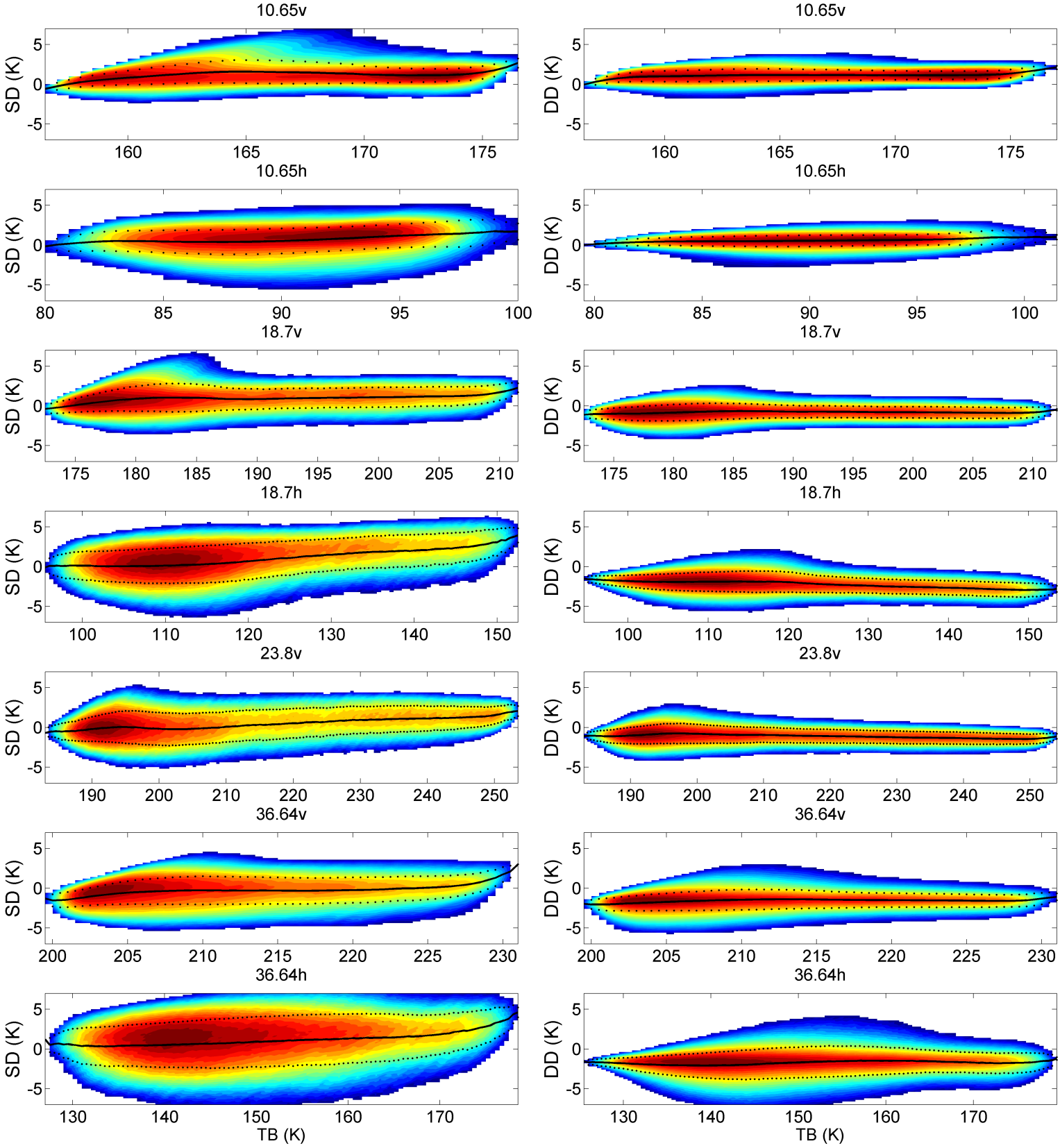

10^3 10^4